

Comprehensive analysis of a dense sample of FRB 121102 bursts

KSHITIJ AGGARWAL ,^{1,2} DEVANSH AGARWAL ,^{1,2} EVAN F. LEWIS ,^{1,2} RESHMA ANNA-THOMAS ,^{1,2}
 JACOB CARDINAL TREMBLAY ,^{1,2} SARAH BURKE-SPOLAOR ,^{1,2,3} MAURA A. MC LAUGHLIN ,^{1,2} AND
 DUNCAN R. LORIMER 

¹ *West Virginia University, Department of Physics and Astronomy, P. O. Box 6315, Morgantown, WV, USA*

² *Center for Gravitational Waves and Cosmology, West Virginia University, Chestnut Ridge Research Building, Morgantown, WV, USA*

³ *CIFAR Azrieli Global Scholars program, CIFAR, Toronto, Canada*

(Received -; Revised -; Accepted -)

Submitted to ApJ

ABSTRACT

We present an analysis of a densely repeating sample of bursts from the first repeating fast radio burst, FRB 121102. We detected a total of 133 bursts in 3 hours of data at a center frequency of 1.4 GHz using the Arecibo Telescope, and develop robust modeling strategies to constrain the spectro-temporal properties of all the bursts in the sample. Most of the burst profiles show a scattering tail, and burst spectra are well modeled by a Gaussian with a median width of 230 MHz. We find a lack of emission below 1300 MHz, consistent with previous studies of FRB 121102. We also find that the peak of the log-normal distribution of wait times decreases from 207 s to 75 s using our larger sample of bursts. Our observations do not favor either Poissonian or Weibull distributions for the burst rate distribution. We searched for periodicity in the bursts using multiple techniques, but did not detect any significant period. The cumulative burst energy distribution exhibits a broken power-law shape, with the lower and higher-energy slopes of -0.4 ± 0.1 and -1.8 ± 0.2 , with the break at $(2.3 \pm 0.2) \times 10^{37}$ ergs. We provide our burst fitting routines as a python package BURSTFIT^a). All the other analysis scripts and results are publicly available^b).

Keywords: Radio transient sources(2008) — Extragalactic radio sources(508) — Radio bursts(1339)
 — Astronomy data analysis(1858) — Markov chain Monte Carlo(1889) — Observational astronomy(1145)

1. INTRODUCTION

Repeating sources of fast radio bursts (FRBs) have helped broaden the horizons of FRB astronomy since their discovery (Spitler et al. 2014, 2016; CHIME/FRB Collaboration et al. 2019). FRB 121102 was first detected in the PALFA survey using the Arecibo telescope, and ten repeat bursts were later detected during targeted observations of the source. While FRB 121102 remains the most extensively observed and studied repeater, to date, 24 repeaters have now been reported

(Petroff & Chatterjee 2021). Moreover, two of these repeating FRBs (FRB 121102 and FRB 180916) show long-term (i.e., days to months) periodicity in their activity (Aggarwal et al. 2020; Rajwade et al. 2020b; Pastor-Marazuela et al. 2020). Some FRBs have also been localized to a variety of host galaxies, ranging from dwarf galaxies to massive elliptical galaxies to luminous spiral galaxies (Heintz et al. 2020).

Both repeating and non-repeating FRBs show a variety of spectro-temporal features and polarization properties: frequency modulation, sub-millisecond structure, drifting sub-pulses, varying polarization position angle, etc (Shannon et al. 2018; Farah et al. 2019; Luo et al. 2020). Detection of multiple bursts from repeaters (like FRB 121102) have facilitated detailed studies of their properties and their environment. However, even after extensive follow-up and detection of hundreds of bursts

Corresponding author: Kshitij Aggarwal
 ka0064@mix.wvu.edu

^a) <https://github.com/thepebteproject/burstfit>

^b) <https://github.com/thepebteproject/FRB121102>

from FRB 121102, the intrinsic emission mechanism remains uncertain, and many progenitor models have been proposed to explain the observational results. As theoretical models lack robust predictions for the observed properties of bursts, several empirical techniques have been employed to model the observed properties of the bursts. Some of those are: (1) using Weibull and Poisson distributions to model the clustering of repeater bursts; (2) using a truncated and broken power-law to model the flux-density distribution; (3) using 2D Gaussians to model the burst spectro-temporal properties; (4) using Gaussians convolved with an exponential tail to model scattering; (5) using a statistical spectral index to compare burst rates at multiple frequencies; (6) using signal-to-noise and structure to maximize DM, etc. (for further details, see [Cruces et al. 2020](#); [Pastor-Marazuela et al. 2020](#); [Gourdji et al. 2019](#); [Hessels et al. 2019](#); [Gajjar et al. 2018](#)).

In view of all these considerations, it is necessary to detect and carefully investigate a large number of bursts from the repeaters to improve the understanding of their emission mechanism. In this paper, we reanalyze the observations for FRB 121102 previously reported by [Gourdji et al. \(2019\)](#) and present the detection of an additional 93 bursts, for a full sample of 133 bursts in these observations. We detail a thorough burst modeling procedure and report extreme frequency modulation in burst spectra and a dearth of burst emission below 1300 MHz. We present and compare the updated burst energy and wait-time distributions and demonstrate how these estimates change dramatically for an incomplete search. We also perform exhaustive short-period periodicity tests to detect any possible rotational period as predicted by neutron star-based progenitor models.

This paper is laid out as follows: In §2 we briefly discuss the data used in this work and discuss the search and spectro-temporal modeling procedure in §3. We then present our modeling results in §4, followed by a discussion of those results and conclusions in §5 and §6.

2. DATA

The data reported here were originally collected, searched for FRBs, and reported by [Gourdji et al. \(2019\)](#). Here we provide only a brief summary of the data used in this analysis, and refer the reader to [Gourdji et al. \(2019\)](#) for further details. The observations were carried out with the 305-m William E. Gordon Telescope at the Arecibo Observatory with the L-Wide receiver and recorded using the Puerto Rican Ultimate Pulsar Processing Instrument (PUPPI). FRB 121102 was observed with 800 MHz bandwidth at a center frequency of 1375 MHz on MJDs 57644 and 57645 for

5967 s and 5545 s respectively. The data were coherently dedispersed at a dispersion measure (DM) value of 557 pc cm⁻³ during the observations and were recorded with 1.56-MHz channel bandwidth and 10.25- μ s sampling resolution. The data used for this study were further decimated to 12.5-MHz channel bandwidth with 64 total channels and 81.92- μ s sampling interval.

3. METHODS

3.1. *The Petabyte Project*

Characterizing the diversity and event rates of FRBs as a function of observing frequency is critical for understanding their nature, the extreme emission physics responsible for FRB and pulsar emission, and the relationship between these two classes of objects. Many surveys have sought comprehensive estimates of these values, all using different observing frequencies, telescopes, and search algorithms but without characterizing the completeness of their search. The Petabyte Project¹ (TPP) aims to address these issues to provide robust event rate estimates and discoveries in several petabytes of new and archival radio data. TPP will perform a uniform search for FRBs in an unprecedented amount of archival data and better probe transients closer, farther, and at higher radio frequencies than previous searches. Our search will have a robust internal assessment of completeness, allowing us to confidently project the frequency-dependent rates of FRBs and other transients.

TPP will use YOUR (a recursive acronym for “your unified reader”; [Aggarwal et al. 2020](#)) to ingest the data and HEIMDALL ([Barsdell 2012](#))² to search it for single pulses. The deep learning-based classifier FETCH ([Aggarwal et al. 2020a](#))³ is then used to classify the candidates identified by HEIMDALL. The data will be searched up to a DM of 5000 pc cm⁻³ (or more, if possible) and a pulse width of 32 ms. All the candidates above a signal-to-noise ratio (S/N) of 6 classified as astrophysical by FETCH will be manually verified. The maximum DM and the pulse width to be searched is governed by the observing frequency, data resolution, and GPU memory and hence would be dealt with on a case-by-case basis. The data and results presented in this paper were analyzed under TPP, using an early version of the TPP pipeline.

3.2. *Single-Pulse Search*

¹ <https://thepetabyteproject.github.io>

² <https://sourceforge.net/projects/heimdall-astro>

³ <https://github.com/devanshkv/fetch>

Within YOUR, we used `your_heimdall.py` which runs HEIMDALL on the PSRFITS data files collected by PUPPI for the single-pulse search. We used two search strategies: (1) DM range between 450–650 pc cm^{−3} with a DM tolerance⁴ of 1% and (2) DM range between 10–5000 pc cm^{−3} with a tolerance of 25%, with a maximum pulse width of 84 ms in both cases (note that the widest FRB 121102 pulse reported at this frequency had a width of ∼35 ms, see [Cruces et al. 2020](#)). The searches resulted in 1,428 and 11,276 candidates, respectively. For each candidate, we extracted a segment of the data (which we hereafter refer to as a “cutout”) centered at the arrival time as reported by HEIMDALL with a time window equal to twice the dispersion delay using `your_candmaker.py`. We then used spectral kurtosis RFI mitigation with a 3σ threshold ([Nita & Gary 2010](#)) to identify and excise frequency channels corrupted by RFI and used this cleaned data to create dedispersed frequency-time images where a factor of width/2 was used to decimate the time axis. We created the DM–time image by dedispersing the data from zero to twice the reported DM and simultaneously decimating the time axis as above (for more details on the candidate pre-processing, see [Agarwal et al. 2020a](#)). These cutouts are then used by FETCH to label FRBs and RFI, and were also manually verified. In total, we found 133 bursts with DMs consistent with that of FRB 121102 with 93 new bursts as compared to the previously published results. We did not detect any bursts at other DMs. Our search missed one burst, B33, reported by [Gourdji et al. \(2019\)](#), probably because it was weak and narrowband (see Section 5.7 for caveats of our search). Figure 1 shows the dynamic spectra of some of the bursts. Candidate cutouts for all the bursts are available on Github⁵.

3.3. Completeness Limit

We define the completeness limit as the pulse energy (also known as fluence) value above which any burst emitted during the observation would be detected. Determining the completeness limit of any single-pulse search is, therefore, essential to defining the sample of bursts to be used for statistical analyses. The most robust method of determining the completeness limit involves an exhaustive injection analysis. In such analyses, simulated transients (with varying properties) are injected on background data, and by analyzing the tran-

sients that were recovered (or missed), one can determine the completeness limit of a search ([Farah et al. 2019; Agarwal et al. 2020b; Gupta et al. 2021](#)). Such an analysis requires access to a large amount of native-resolution data observed with the same telescope and observing configuration as the search data.

As we had access to decimated data for just two observations, we could not do such an injection analysis. We, therefore, estimate the completeness limit from the radiometer equation. We use a conservative approach by including the effect of RFI mitigation, which reduces search sensitivity. We flagged more than 35% of data for many candidates due to RFI, leading to a usable bandwidth of 500 MHz. Using this smaller bandwidth and nominal pulse width of 1 ms, the fluence limit above an S/N of 8 is 0.0216 Jy ms. We use bursts with fitted fluence above this limit in the burst sample analysis.

3.4. Spectro-temporal Burst Modelling

To measure the properties of the bursts in our sample, we perform spectro-temporal modeling of all the detections. We model each component of the bursts’ spectra with a Gaussian function and the profile using a Gaussian convolved with a one-sided exponential function to represent the Gaussian pulse and the scattering tail. Therefore, we model each component of the burst (at an observing frequency ν and time t), using the following function,

$$\begin{aligned} \mathcal{F}(\nu, t; S, \mu_\nu, \sigma_\nu, \mu_{\text{DM}}, \sigma_t, \tau_{\text{sc}}) = & S \\ & \times \mathcal{P}_\nu(t; \mu_{\text{DM}}, \sigma_t, \tau_{\text{sc}}) \\ & \times \mathcal{G}(\nu; \mu_\nu, \sigma_\nu). \end{aligned} \quad (1)$$

Here, S is the fluence of the component, \mathcal{G} is the Gaussian function to model the spectra

$$\mathcal{G}(x; \mu_x, \sigma_x) = \frac{1}{\sigma_x \sqrt{2\pi}} \exp\left(-\frac{1}{2} \frac{(x - \mu_x)^2}{\sigma_x^2}\right) \quad (2)$$

and \mathcal{P} is used to model the profile. For bursts with scattering, we use the Gaussian convolved with a one-sided exponential function ([McKinnon 2014](#)),

$$\begin{aligned} \mathcal{P}_\nu^{\text{scat}}(t; \mu_{\text{DM}}, \sigma_t, \tau_{\text{sc}}) = & \frac{1}{2\tau_{\text{sc}}} \left\{ 1 + \text{erf} \left[\frac{t - (\mu_{\text{DM}} + \sigma_t^2/\tau_{\text{sc}})}{\sigma_t \sqrt{2}} \right] \right\} \\ & \times \exp \left(\frac{\sigma_t^2}{2\tau_{\text{sc}}^2} \right) \exp \left(\frac{t - \mu_{\text{DM}}}{\tau_{\text{sc}}} \right). \end{aligned} \quad (3)$$

where the mean of the Gaussian pulse after accounting for the dispersion delay at that respective frequency,

$$\mu_{\text{DM}} = \mu_t - 4.148808 \times 10^3 \text{ DM} \left(\frac{1}{\nu^2} - \frac{1}{\nu_{\text{top}}^2} \right) \text{ s.} \quad (4)$$

Here ν_{top} is the highest frequency in the band (in MHz), ν is the frequency of a channel (in MHz) and μ_t is the

⁴ DM tolerance is the acceptable sensitivity loss between DM trials for a single-pulse search (for further details, see [Agarwal et al. 2021; Levin 2012](#))

⁵ <https://github.com/theptabteproject/FRB121102>

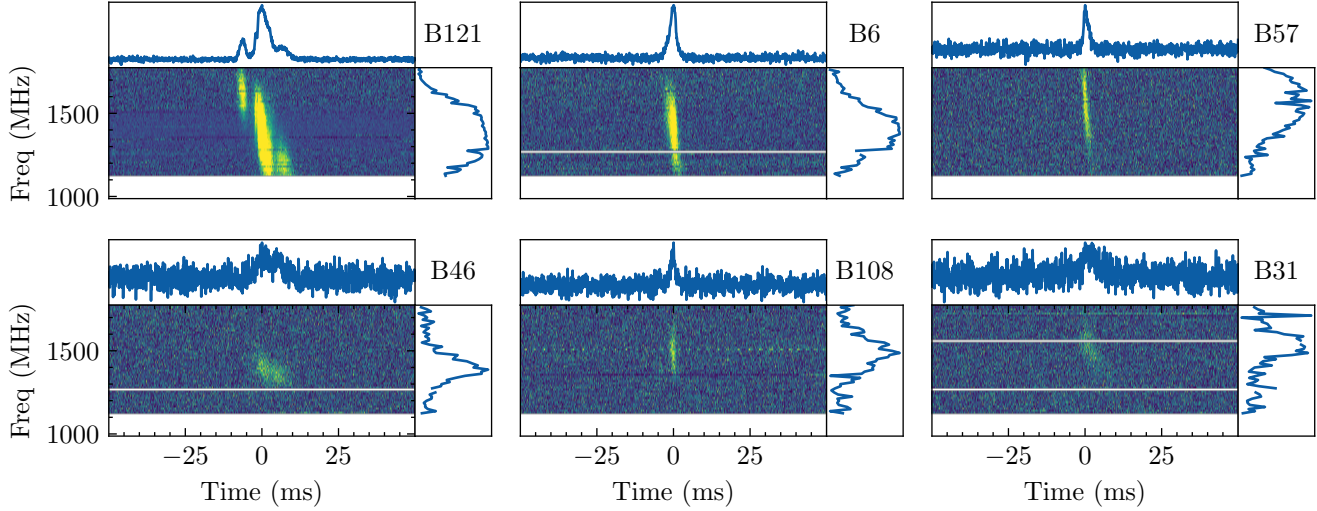


Figure 1. Dynamic spectra of six bursts, dedispersed at $DM = 560.5 \text{ pc cm}^{-3}$. For each burst, the top panel shows the burst profile obtained by averaging along the frequency axis, and the right panel shows the burst spectra obtained by averaging the burst data along the time axis. The white horizontal lines show the channels masked due to RFI. The color scale of each spectrogram has been set from mean to 3 times the standard deviation of the off-pulse region. The ranges of 1D plots are different for individual plots. Burst numbers are mentioned on the top right of each subplot.

mean of the Gaussian pulse at ν_{top} . At each frequency channel, the scattering time scale

$$\tau_{\text{sc}}(\nu) = \tau_{\text{sc}} \left(\frac{\nu}{\nu_{\text{ref}}} \right)^{-4}. \quad (5)$$

In this expression, ν_{ref} is the reference frequency and is set to be 1 GHz. The exponent (-4) is assuming a normal distribution of plasma-density inhomogeneities. Finally, we defined $\mathcal{P}_\nu(t; \mu_{\text{DM}}, \sigma_t, \tau_{\text{sc}})$ to be a Gaussian $\mathcal{G}(t; \mu_{\text{DM}}, \sigma_t)$ for $\tau_{\text{sc}}/\sigma_t < 6$, and $\mathcal{P}_\nu^{\text{scat}}(t; \mu_{\text{DM}}, \sigma_t, \tau_{\text{sc}})$ for $\tau_{\text{sc}}/\sigma_t > 6$. We used this value for the cutoff in order to maintain numerical stability while calculating Equation 3.

It follows from the above discussion that our model \mathcal{F} is generated using seven parameters: $S, \mu_\nu, \sigma_\nu, \mu_t, \sigma_t, \tau_{\text{sc}}$ and DM. Using this model we fit the burst spectrograms, as described in the next section.

3.5. BURSTFIT

While fitting for complex FRB bursts is an arduous task, we scrupulously automate the entire procedure and present it as python package BURSTFIT⁶. BURSTFIT provides a framework to model any spectrogram consisting of any complex FRB or pulsar pulse using robust methods. It can easily incorporate any user-defined python function(s) to model the profile, spectra, and spectrogram and is not limited to the functions we have implemented for this current analysis. BURSTFIT primarily consists of the following five steps.

⁶ <https://github.com/theptabyteproject/burstfit>

3.5.1. Data Preparation

First, we dedispersed the burst spectrogram at the DM obtained from the single-pulse search. This DM is usually accurate enough to correct for most of the dispersion. We cut out a time window of 200 ms encompassing the burst from this dedispersed spectrogram and normalized this data to zero mean and unit standard deviation using the off-pulse region. Both the cutout and normalized data were then used for fitting. We also masked all the channels flagged as RFI during the search and candidate pre-processing so as not to influence the fitting procedure.

3.5.2. Stage 1: Single-component Fitting

In this first stage of fitting, we used `scipy.curve_fit`⁷ to perform the fits and got an initial estimate of the fitted parameters. We created the time-series profile by summing along the frequency axis, and modelled it using $S \times \mathcal{P}_\nu(t; \mu_t, \sigma_t, \tau_{\text{sc}})$. We then used the fitted values of μ_t and σ_t to identify the time samples with the burst signal and average them to produce the burst spectra. We normalised this spectra to unit area, and modelled it using $\mathcal{G}(\nu; \mu_\nu, \sigma_\nu)$. Following this, we modelled the complete spectrogram. We first generated the model spectrogram by stacking N_ν model pulse profiles ($S \times \mathcal{P}_\nu(t; \mu_{\text{DM}}, \sigma_t, \tau_{\text{sc}})$) together, where N_ν is the number of frequency channels. Note that the mean of each

⁷ This routine is a part of the python-based `scipy` package. We used version 1.5.2 of this package in our analysis.

profile was already corrected for the dispersion delay at that respective frequency. This gave us a scattered and dispersed spectrogram at a given set of profile parameters and a DM.

We then multiplied this spectrogram with the model spectra to obtain the model spectrogram. Additionally, we clipped the model spectrogram at the estimated saturation level (see Section 3.5.6) and masked the RFI channels. Using this model we fit for all the seven parameters in $\mathcal{F}(\nu, t; S, \mu_\nu, \sigma_\nu, \mu_t, \sigma_t, \tau_{sc})$ along with DM by comparing the model with the dedispersed cutout spectrogram obtained in the previous step. Again, we used `scipy.curve_fit` for fitting, and used the estimates from individual profile and spectra fits as initial guesses for the parameters.

3.5.3. Stage 2: Statistical Tests

Following Stage 1, we obtained the residual spectrogram by subtracting the fitted model from the original spectrogram. Then we performed several statistical tests (see, e.g., Kramer et al. 1994) to compare the properties of on-pulse residual with respect to the off-pulse regions in the original spectrogram. We performed the following three comparisons: left off-pulse vs. right off-pulse, on-pulse vs. left off-pulse, and on-pulse vs. right off-pulse. We used the following four tests (all implemented within `scipy`): Kolmogorov–Smirnov test (for distribution comparison), F-test (for variance comparison), T-test (for mean comparison), and Kruskal test (for median comparison).

We considered the two distributions similar if at least two of the four tests had a *p*-value above 0.05 (i.e. we did not have significant support for the non-similarity of the distributions). Comparing left off-pulse with right off-pulse region gave us confidence in our choice of off-pulse region. We terminated the single component fitting procedure if either of the off-pulse vs. on-pulse comparisons demonstrates that the distributions are similar. If the distributions were different, we used the residual spectrogram and repeated Stage 1 and 2 to fit another component and compared the on-pulse residual with off-pulse data. We kept fitting for components until the statistical tests pass or until a maximum of five components is reached.

3.5.4. Stage 3: Multi-component Fitting

In cases where multiple components were found, we performed another stage of the fitting. Here, we generated a combined model consisting of all the components and fit for all components by comparing our model with the original spectrogram. This combined model (\mathcal{F}_{all}) was generated by summing together the individual com-

ponent models (\mathcal{F}_i) for all N components,

$$\mathcal{F}_{all} = \sum_i^N \mathcal{F}_i. \quad (6)$$

Again, we used `scipy.curve_fit` for fitting. Here, the fit results of the individual component fits from previous stages were used as the initial guess for the parameters in `curve_fit`.

3.5.5. Stage 4: MCMC

While `scipy.curve_fit` is sufficient for fitting in many scenarios, in our testing we found that the estimates and the errors reported by `scipy.curve_fit` were not robust for our purposes. In many cases, the errors reported by `scipy.curve_fit` were possibly underestimated, and fitted results were highly susceptible to the choice of input parameter bounds. This was especially true for low-significance bursts and multiple-component bursts, where the least-squares-minimization technique struggles to find a good solution. Therefore, we added another stage to our fitting procedure and used a Markov Chain Monte Carlo (MCMC) to obtain the final fitting results. We used the results of previous stages (that used `scipy.curve_fit`) as initial estimates to determine the starting positions of the walkers for the MCMC. An advantage of the MCMC procedure is that it provides the full posterior distribution of all the fitted parameters, which we could then use to estimate the errors and further follow-up analysis of the burst sample. We used the Goodman and Weare affine invariant sampler (Goodman & Weare 2010) as implemented in EMCEE (Foreman-Mackey et al. 2013). We used uniform priors for all the parameters, with the ranges of the priors given in Table 1. We used the log-likelihood function

$$\ln \mathcal{L} = -0.5 \sum \left(\frac{\mathcal{S} - \mathcal{F}_{all}}{\sigma} \right)^2, \quad (7)$$

where \mathcal{S} refers to the original spectrogram, \mathcal{F}_{all} refers to the model, and σ is the off-pulse standard deviation of the measured spectrogram. The sum is over all the pixels in the two spectrograms. We used autocorrelation analysis to determine when the MCMC has converged⁸. We then estimated the burn-in using the autocorrelation time and used the remaining samples to determine the fitting results. To decide if scattering was present in a burst, we used the percentage of samples with $\tau_{sc}/\sigma_t < 6$. If this percentage was greater than 50%,

⁸ See <https://emcee.readthedocs.io/en/stable/tutorials/autocorr> for details.

Table 1. Priors used in the MCMC fitting

Parameter	Minimum	Maximum
S	0	$500 \times \max(\text{time_series}) \times \sigma_t^{\text{fit}}$
μ_{ν}	$-2 \times N_{\nu}$	$3 \times N_{\nu}$
σ_{ν}	0	$5 \times N_{\nu}$
μ_t	$0.8 \times \mu_t^{\text{fit}}$	$1.2 \times \mu_t^{\text{fit}}$
σ_t	0	$1.2 \times (\sigma_t^{\text{fit}} + \tau_{\text{sc}}^{\text{fit}})$
τ_{sc}	0	$1.2 \times (\sigma_t^{\text{fit}} + \tau_{\text{sc}}^{\text{fit}})$
DM	$0.8 \times \text{DM}^{\text{fit}}$	$1.2 \times \text{DM}^{\text{fit}}$

NOTE—Superscript fit refers to the values obtained using fits done in previous stages. N_{ν} refers to the number of frequency channels. `time_series` refers to the 1-D array obtained by summing the dedispersed cutout spectrogram along the frequency axis. Subscripts t and ν are used for profile and spectra parameters.

we concluded that scattering was not present (or was very small) in that burst. We do not report scattering timescales for such bursts.

We generated corner plots and fit-result plots to verify the quality of the fits, as shown in Figures 3 and 4. We provide all the results (output parameters, corner plots, fitting-result plots, etc.) from our analysis in a Github repository.⁹

3.5.6. Handling data saturation

The data we use in this analysis were recorded as 8-bit unsigned integers. Hence, the data range lies between 0–255, and any signal brighter than 255 is clipped at this value. We noticed data saturation for several bursts, and hence this effect has been incorporated in our burst modeling. The spectrograms are subtracted by the off-pulse mean (μ_{off}) and divided by the off-pulse standard deviation (σ_{off}). While making the spectro-temporal model, we clip the values greater than $(255 - \mu_{\text{off}})/\sigma_{\text{off}}$. This effect is visible in Figure 2 for burst B121 where the red dot-dashed curve and green dotted curve show the fit to the burst spectra with and without clipping, respectively. The fit performed without considering the saturation underestimates the burst's spectral width, leading to an underestimated burst energy.

3.5.7. Caveats to our fitting analysis

There are some caveats to our fitting procedure that are worth noting here. First, as with any model-dependent fitting, our analysis and results are dependent on the choice of the functions we use to model the data. We described those functions and our motivation

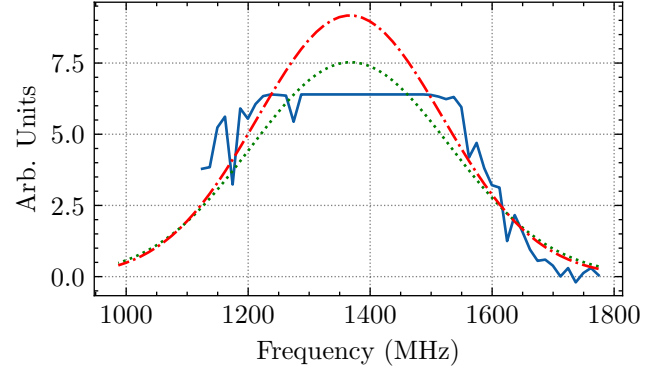


Figure 2. Plots of spectra and fits in case of data saturation. Blue solid line shows the spectrum of burst B121. The spectrum shows saturation between 1250 MHz and 1550 MHz, and any real structure in the spectrum is lost between those frequencies. The red dot-dashed line shows the model spectrum obtained when the fitting procedure incorporates the effect of saturation, while the dotted green line shows the spectrum obtained without considering saturation. The red curve better estimates the shape of the spectrum (assuming that the spectrum can be modeled using a Gaussian function), while the green curve underestimates the fluence and frequency width. See § 3.5.6 for more details.

for using them in Section 3.4, but these are not the only proposed methods to model the spectrogram of an FRB. The spectrum of an FRB can also have power-law-like behavior (CHIME/FRB Collaboration et al. 2020), and some other pulse broadening functions can also be used besides the exponential tail used to model the scattering effect (Bhat et al. 2004).

Second, the emission of some bursts in our sample was present only in the top part of the band. In many such cases, the emission appeared similar to the tail of a Gaussian function, with the mean lying outside our observing band. Although we allowed for such a mean value to be estimated with the MCMC procedure, our fitting results for such bursts would inevitably be unconstrained. We therefore mark such bursts with a † in Table 2 to highlight this.

Third, in some cases, the MCMC procedure was unable to find a robust solution. This was due to the presence of RFI, which could not be removed as the FRB signal coincided with the channels heavily corrupted by RFI. It also occurred when there was significant baseline variation in the data close to a weak FRB pulse. This could dominate the MCMC likelihood estimate, and therefore the procedure could not converge on a solution. For such cases, we only used `scipy.curve.fit` to perform the fits, and we modified the fitting bounds to obtain a visually good fit. We highlight these in Table 2 with *, and note that the values could be unreliable.

⁹ <https://github.com/thepebyteproject/FRB121102>

4. RESULTS

As mentioned previously, we tripled the number of published bursts from these two observations to 133, by detecting 93 new bursts. Dynamic spectra for some of the high-significance bursts are shown in Figure 1.

We used the burst modeling procedure described in the previous sections to estimate spectral and temporal properties for all the bursts. Figure 3 shows the fitting results for two bursts. Comparing the three columns, we can see that the modeled bursts look similar to the original burst signal and the residuals are noise-like, indicating that the models assumed for the burst spectrogram provide satisfactory fits. Figure 4 shows the posterior distribution of the burst properties obtained using MCMC for B67. The 1D plots show the parameter histogram, while the 2D plots show correlations between parameters. The properties of the bursts are given in Table 2.

4.1. Burst sample properties

We used the converged sample chains from the MCMC fitting for each burst to generate a cumulative corner plot with the whole burst sample properties. To do this, we randomly selected 1000 samples from the final 25% of the MCMC chains and then concatenated such samples from all the bursts. We then generated a corner plot using these samples, as shown in Figure 5¹⁰. We can now use Figure 5 to infer trends in various spectro-temporal properties of FRB 121102. Table 3 shows the summary statistics of all the bursts obtained from this analysis. We can see that the spectra of the bursts typically peak around 1650 MHz, and there is a dearth of burst emission below 1300 MHz. Most of the burst spectra peak within the top part of our observing band (i.e 1550–1780 MHz). This behavior possibly extends further to higher frequencies, as is evident from many burst spectra that increase towards the top part of the observing band with their spectral peak possibly lying outside our observing band. Interestingly, [Platts et al. \(2021\)](#) have recently reported complex bifurcating structures in some FRB 121102 bursts below 1250 MHz using higher-resolution data. It is, therefore, possible that the emission of FRB 121102 shows a different behavior below these frequencies, which might also vary with time.

As already noted by [Gourdji et al. \(2019\)](#), FRB 121102 shows a variety of spectral widths. Using our modeling, we observe that most bursts are frequency-modulated

and have a typical frequency width of ~ 230 MHz. The bursts also show a wide range of intrinsic pulse widths, from 0.4 ms to 20 ms, and various scattering timescales, up to 3 ms. The median dispersion measure of the bursts we observe was 564 pc cm^{-3} , with a 1σ variation of $\sim 4 \text{ pc cm}^{-3}$. This variation in DM is also apparent in Figures 5 and 6. This value is consistent with the other published estimates ([Gourdji et al. 2019](#); [Cruces et al. 2020](#); [Platts et al. 2021](#)). We also did not see any strong correlation between any two burst properties from Figure 5. Several of the bursts from this sample also show the characteristic sub-burst drift in frequency during the burst duration, sometimes referred to as the “sad-trombone” effect ([Hessels et al. 2019](#)). We did not detect any evidence of upward drifting as predicted by some FRB models ([Cordes et al. 2017](#)), and reported by [Platts et al. \(2021\)](#).

Many bursts in our sample show multiple components, and we estimated the properties of these components using our fitting procedure. Nine bursts in our sample show two components, while there is one burst with three components (see Table 2). We also note that it is difficult to differentiate between multiple closely spaced bursts and different components from single bursts. This is further complicated by the detection of a very wide (~ 35 ms) burst reported by [Cruces et al. \(2020\)](#). As there is no clear consensus on how to resolve this, we visually identified some bursts as components of a nearby burst and reported them as such in Table 2. We consider all the components as individual bursts for all the following analysis except the cumulative energy distribution analysis.

Figure 6 shows the scatter plots of various burst properties with respect to the burst time. The bursts from two observations are shown in different colors, and the time is referenced to the first burst of the respective observation. The bursts properties do not show any temporal evolution at the seconds-to-minutes time scale. We also did not observe any distinction between the distribution of properties of bursts detected on two consecutive days.

5. DISCUSSION

5.1. Cumulative energy distribution

Energy distributions can provide useful intuition into the emission mechanism of the source. Regular pulsar emission typically shows a log-normal distribution, whereas giant pulses show power-law cumulative distributions ([Burke-Spolaor et al. 2012](#)). Crab giant pulses have power-law indices γ ranging from roughly -1 to -3 at frequencies near 1.4 GHz, and show evidence that the index depends on pulse width and energy, with flat-

¹⁰ Note that this corner plot is different from the one in Figure 4. Figure 4 shows the samples from MCMC fit on only one burst, while Figure 5 shows the cumulative samples obtained from MCMC fit on all the bursts.

Table 2. Properties of the first 10 bursts. See Appendix for the full table.

Burst	^a ID	μ_f (MHz)	σ_f (MHz)	S (Jy ms)	μ_t ^b (MJD)	σ_t (ms)	τ (ms)	DM (pc cm ⁻³)
B1*	1560 ⁺³⁰ ₋₃₀	210 ⁺⁴⁰ ₋₄₀	0.09 ^{+0.02} _{-0.02}	57644.408906976(1)	0.0 ^{+0.02} _{-0.02}	1.9 ^{+0.3} _{-0.3}	565.3 ^{+0.4} _{-0.4}	
B2*	1200 ⁺¹⁰ ₋₁₀	50 ⁺¹⁰ ₋₁₀	0.043 ^{+0.007} _{-0.007}	57644.40956768(1)	1.35 ^{+0.05} _{-0.05}	-	562.4 ^{+0.8} _{-0.8}	
B3.1†	2900 ⁺³⁰⁰ ₋₆₀₀	800 ⁺³⁰⁰ ₋₂₀₀	0.6 ^{+0.7} _{-0.3}	57644.409673699(3)	0.4 ^{+0.2} _{-0.2}	1.3 ^{+0.7} _{-0.7}	566.8 ^{+0.8} _{-0.9}	
B3.2†	1100 ⁺³⁰⁰ ₋₁₄₀₀	1000 ⁺²⁰⁰⁰ ₋₁₀₀₀	0.09 ^{+0.13} _{-0.04}	57644.40967384(2)	0.3 ^{+1.4} _{-0.2}	0.3 ^{+0.7} _{-0.1}	564.7 ^{+1.5} _{-0.4}	
B4†	3100 ⁺²⁰⁰ ₋₆₀₀	550 ⁺⁸⁰ ₋₁₁₀	2 ⁺⁴ ₋₂	57644.410072889(4)	1.1 ^{+0.2} _{-0.2}	0.3 ^{+0.2} _{-0.1}	564 ⁺¹ ₋₁	
B5†	2100 ⁺⁹⁰⁰ ₋₁₆₀₀	2700 ⁺⁹⁰⁰ ₋₁₂₀₀	0.19 ^{+0.05} _{-0.04}	57644.410157834(4)	0.7 ^{+0.3} _{-0.3}	1.0 ^{+0.4} _{-0.3}	562.1 ^{+0.7} _{-0.6}	
B6.1	1393 ⁺⁷ ₋₇	183 ⁺⁷ ₋₇	0.47 ^{+0.02} _{-0.03}	57644.411071954(1)	1.09 ^{+0.03} _{-0.04}	-	562.3 ^{+0.2} _{-0.1}	
B6.2	1417 ⁺⁴ ₋₅	102 ⁺⁵ ₋₄	0.33 ^{+0.03} _{-0.02}	57644.4110719755(9)	0.57 ^{+0.03} _{-0.02}	-	560.9 ^{+0.2} _{-0.1}	
B7.1†	3100 ⁺²⁰⁰ ₋₃₀₀	430 ⁺⁶⁰ ₋₈₀	10 ⁺²⁰ ₋₁₀	57644.412240214(5)	0.7 ^{+0.3} _{-0.4}	0.8 ^{+0.4} _{-0.4}	569 ⁺³ ₋₃	
B7.2†	1460 ⁺²⁰ ₋₂₀	90 ⁺³⁰ ₋₂₀	0.09 ^{+0.01} _{-0.01}	57644.41224043(2)	1.9 ^{+0.9} _{-1.0}	1.2 ^{+0.6} _{-0.5}	569 ⁺³ ₋₂	
B8†	3000 ⁺²⁰⁰ ₋₆₀₀	700 ⁺¹⁰⁰ ₋₁₀₀	1.1 ^{+1.5} _{-0.7}	57644.414123628(4)	1.0 ^{+0.3} _{-0.3}	0.8 ^{+0.4} _{-0.3}	567.5 ^{+0.9} _{-0.7}	
B9*	1430 ⁺¹⁰ ₋₁₀	75 ⁺⁹ ₋₉	0.076 ^{+0.003} _{-0.003}	57644.41447161(2)	2.0 ^{+0.6} _{-0.6}	0.4 ^{+0.6} _{-0.6}	564 ⁺² ₋₂	
B10	1630 ⁺¹⁰ ₋₁₀	82 ⁺⁸ ₋₈	0.1 ^{+0.01} _{-0.01}	57644.414475391(7)	1.4 ^{+0.3} _{-0.3}	0.5 ^{+0.3} _{-0.2}	562 ⁺³ ₋₃	

NOTE— 1σ errors on the fits are shown on superscript and subscript of each value in the table. For μ_t , the error on the last significant digit is shown in parenthesis.

^aBurst IDs are chronological. Individual component number (N) for multi-component bursts are appended to the burst IDs. Bursts modeled only using `curve_fit` are marked with *. We do not show the errors on these bursts as we found them to be unreliable and are under or overestimated. Bursts that extend beyond the observable bandwidth can also have unreliable estimates of spectra parameters and fluence (see Section 3.5.7). We mark those bursts with † to indicate that their fluence and spectra parameters could be unconstrained.

^b μ_t is the mean of the pulse profile in units of MJD. This can be considered as the arrival time of the pulse. It is referenced to the solar system barycenter, after correcting to infinite frequency using a DM of 560.5 pc cm⁻³.

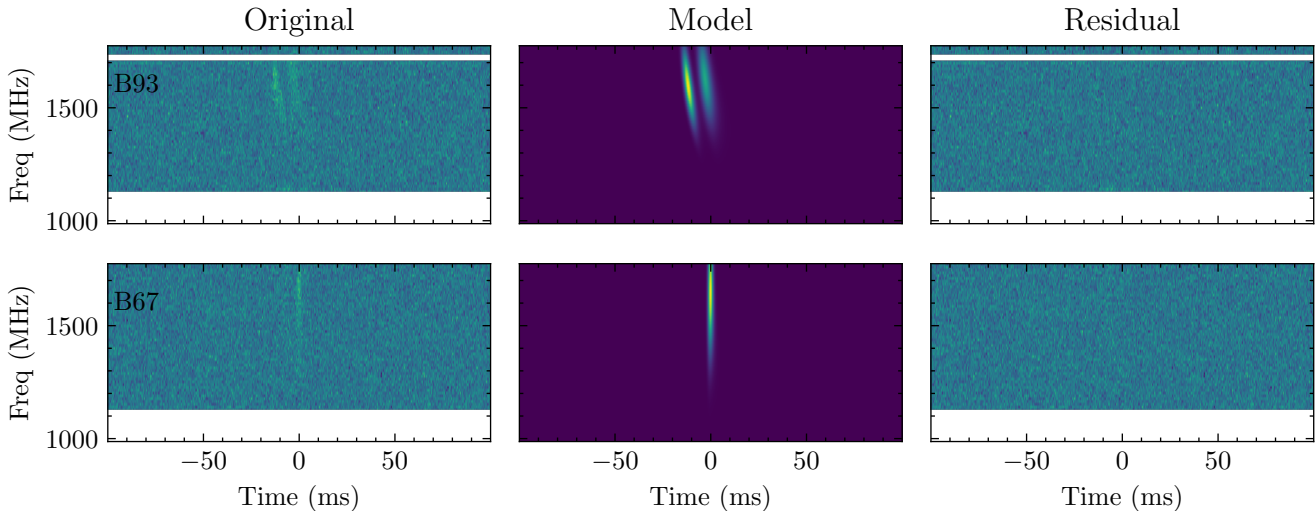


Figure 3. Results of spectro-temporal fits on two bursts (B93 and B67). The first column shows the original (normalized) dynamic spectra of the bursts. The burst can be seen in both cases towards the top of the band. B93 shows two components, separated by around 10 ms. The middle column shows the noise-free model spectrograms that best fit the original data. The last column shows the residual spectrogram obtained by subtracting the model from the original data. The residual spectrogram in both cases shows noise-like data with no remaining artifacts. See Section 3.5 for details of the fitting procedure.

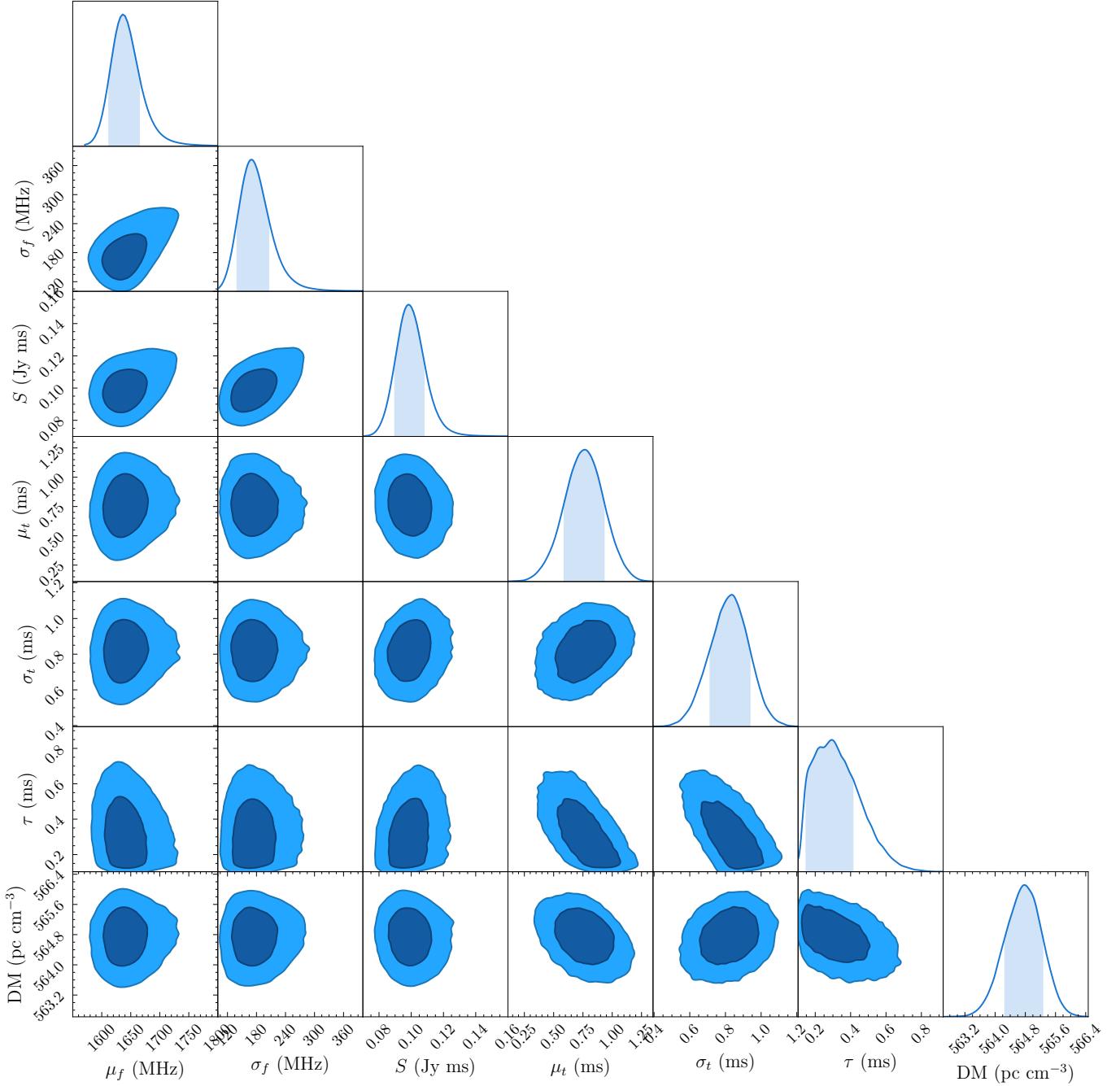


Figure 4. Corner plot generated using the MCMC samples obtained after fitting B67. The 1D histograms show the histogram of individual parameters, while the 2D plots show the correlations between parameters. The shaded and darkened region in 1D and 2D plots correspond to 1σ . μ_t is in units of milliseconds and is with respect to MJD=57645.41732241795. The value of μ_t is referenced to the observatory site (Arecibo Observatory) and at the top of the frequency band i.e. 1774.53125 MHz. See Sections 3.5 and 4 for more details.

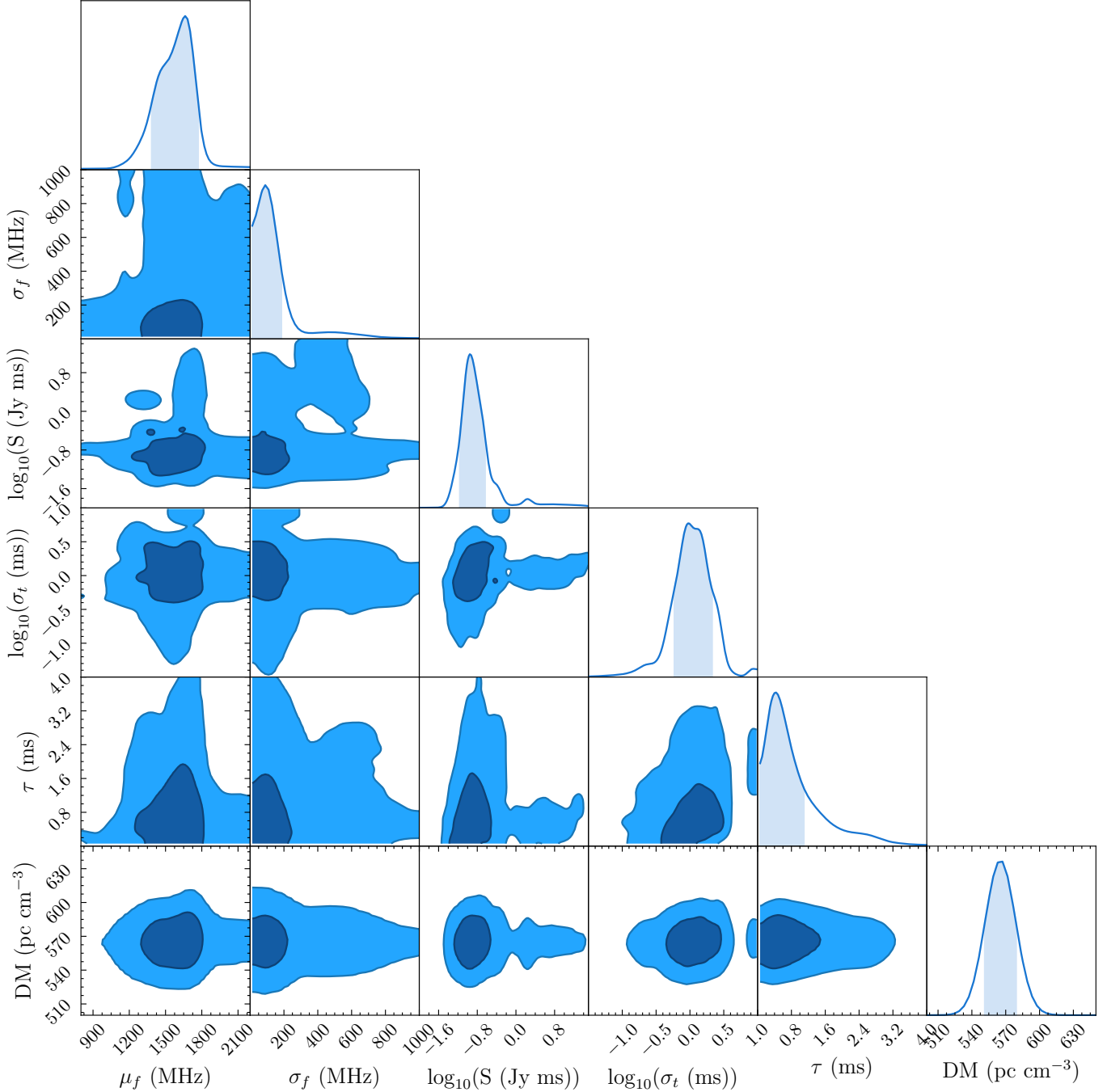


Figure 5. Corner plot generated using samples from the MCMC fit for all the bursts. The 1D histograms show the distribution of individual parameters for all the FRB 121102 bursts, while the 2D plots show the correlations for different parameters. The shaded and darker regions in 1D and 2D plots correspond to 1σ . See Section 4 for more details.

ter indices for weaker and shorter pulses (Karuppusamy et al. 2010; Popov & Stappers 2007; Bera & Chengalur 2019). High-energy magnetar emission has been described by power-law distributions with γ ranging from roughly -1.6 to -1.8 (Cheng et al. 2020). Previous studies of FRB 121102 energy distributions have used a single power-law fit ($N \propto E^\gamma$) to model the cumulative distribution and have obtained different values of γ

ranging from -0.7 in Law et al. (2017), -1.1 in Cruces et al. (2020), -1.7 in Oostrum et al. (2020) and -1.8 in Gourdji et al. (2019). Another well-studied repeating source, FRB 180916, shows $\gamma = -1.3$ at 400 MHz, although recent observations have reported a flattening of the power-law at lower energies (Chime/Frb Collaboration et al. 2020; Pastor-Marazuela et al. 2020).

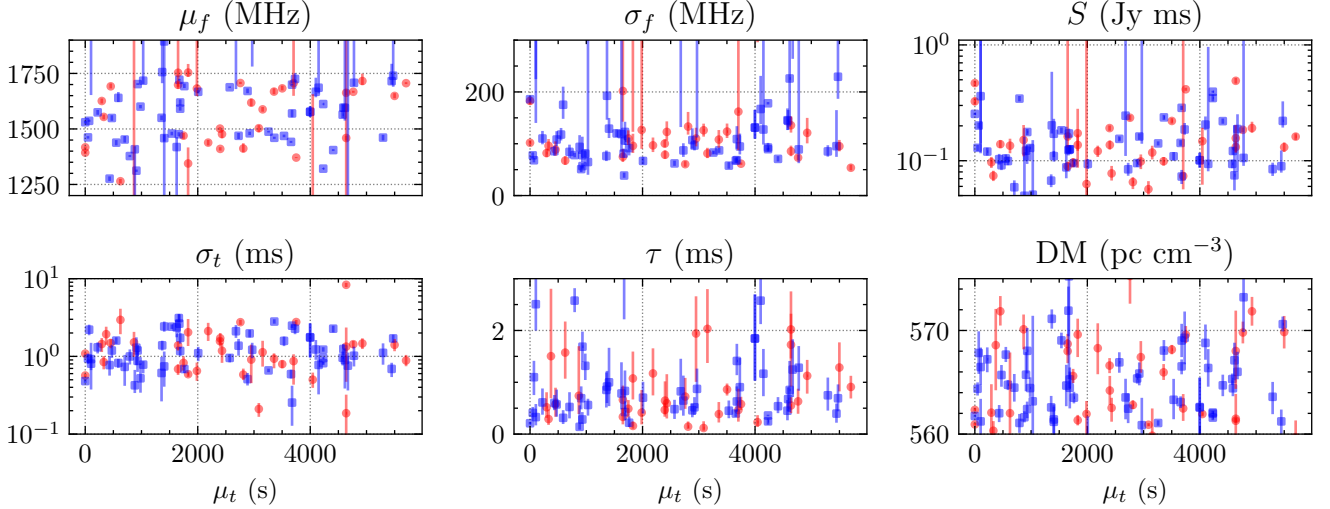


Figure 6. Scatter plots of fitted property of the bursts versus the fitted time of the burst. The data from the two observations are shown in different colors, with MJD 57644 in red and MJD 57645 in blue. μ_t is referred to the first detected burst in the observation. Only bursts fit using MCMC are shown here. The error bars represent 1σ errors on the fit. Errors on μ_t are very small, and hence are not visible. None of the six properties show any clear trend with respect to the burst time.

Table 3. Results from the burst sample analysis. The values represent the median values with 1σ errors.

Parameter	Units	Value
μ_f	MHz	1608^{+100}_{-200}
σ_f	MHz	102^{+130}_{-30}
S	Jy ms	$0.13^{+0.13}_{-0.05}$
σ_t	ms	$1.1^{+0.9}_{-0.5}$
τ	ms	$0.7^{+0.9}_{-0.4}$
DM	pc cm $^{-3}$	564^{+5}_{-3}

We calculate the isotropic energy (E) of a burst as,

$$E = 4\pi D_L^2 \times S (\text{Jy s}) \times 2.355 \sigma_\nu (\text{Hz}) \times 10^{-23} (\text{ergs}^{-1} \text{cm}^{-2} \text{Hz}^{-1}). \quad (8)$$

Here, D_L is the luminosity distance to FRB 121102, 972 Mpc, as reported by Tendulkar et al. (2017). S and $2.355 \sigma_\nu$ are the fitted fluence and FWHM of the Gaussian spectra.

To make the cumulative energy distribution, we choose only bursts for which the $\pm 1\sigma$ bounds on the spectral peak fell within our observing band. This was done as our fluence estimates obtained from fitting are reliable for bursts within our band and because we are incomplete to the population of bursts that are partially outside our band (K. Aggarwal et al. 2021, in prep). From this sample of 60 bursts, we bootstrap the cumulative energy distribution by randomly drawing one

point from their energy distribution. In order to get a distribution, this process is repeated 1000 times. We used `scipy.curve_fit` to fit each of these 1000 energy distributions with a broken power law of the form,

$$N(\geq E) = \begin{cases} E_{\text{scale}} \left(\frac{E}{E_{\text{break}}} \right)^\alpha, & \text{if } E < E_{\text{break}} \\ E_{\text{scale}} \left(\frac{E}{E_{\text{break}}} \right)^\beta, & \text{if } E > E_{\text{break}} \end{cases} \quad (9)$$

Here, α and β are the two power law indices, E_{break} is the break energy, and E_{scale} is the energy scaling. Figure 7 shows the cumulative energy distributions above an estimated completeness of 5.81×10^{36} ergs, calculated from the aforementioned completeness limit on the fluence (Section 3.3) and median bandwidth of the bursts. It also shows (in red) the power-law fit to each cumulative energy distribution.

The median of the distribution of fitted power-law indices and break energy (with 1σ errors) are given by $\alpha = -0.4 \pm 0.1$, $\beta = -1.8 \pm 0.2$ and $E_{\text{break}} = (2.28 \pm 0.19) \times 10^{37}$ ergs. This break at E_{break} could indicate the actual completeness energy limit of our observations, and we might therefore be incomplete to the bursts with energies below E_{break} . This could be due to the incompleteness of our observations to the weak, band-limited bursts. The break in energy distribution has also been reported for other repeating FRBs (Pastor-Marazuela et al. 2020). It is worth noting that our higher-energy power-law index β is also consistent with the power-law index estimated by Gourdji et al. (2019) above a completeness threshold of 2×10^{37} ergs. In the context of pulse-energy distributions, the similar-

ity of the power-law indices of FRB 121102 with both those of Crab giant pulses and magnetar pulses might also imply a common origin (Lyu et al. 2021). Figure 7 shows that two high energy bursts deviate from the power law fits. This has also been seen in Crab giant pulses, where this behavior was speculated to be due to supergiant pulses (Mickaliger et al. 2012).

5.2. Wait-time distribution

The left panel in Figure 8 shows the distribution of wait times between bursts, which follows a bi-modal distribution as also seen in previous studies (Li et al. 2019; Gourdji et al. 2019). On wait times greater than 1 s, we use `scipy.curve_fit` to fit a log-normal function to the main distribution, finding a peak at 74.8 ± 0.1 s. The peak of our wait-time distribution is significantly lower than the 207 ± 1 s peak found in this data by Gourdji et al. (2019), due to our increased sample of bursts filling in the wait-time gaps. Our findings most closely match the wait-time distribution of Zhang et al. (2018), which peaks at ~ 67 s; while the original paper did not report an exact peak, we used their publicly available data¹¹ to perform our wait-time analysis. These similarities suggest that careful single-pulse searches using machine-learning algorithms allow us to obtain a robust sample of bursts that accurately reflects the burst population.

As in previous studies (e.g., Li et al. 2019; Katz 2018; Gourdji et al. 2019), we find a smaller population of bursts with sub-second separations. However, unlike the previously reported distributions, which cluster around tens of milliseconds, our sub-second burst separations span the range of tens of milliseconds up to nearly one second without a clear break between the two distributions. For this analysis, we assume that each closely spaced pair of bursts is composed of two separate bursts instead of components of a single broader burst, leading to the larger distribution of short wait times compared to other papers. This assumption will not drastically alter the fitted log-normal distribution since the sub-second wait-time population is small, and their removal will not significantly alter the shape of the main distribution. As in Gourdji et al. (2019) and Li et al. (2019), we find that the wait time between bursts and their relative fluences are not correlated.

To quantify the change in the wait-time peak as a function of the number of bursts in a sample, we perform the same wait-time analysis for a random selection of our bursts over a range of burst numbers, as seen in

the right-hand panel of Figure 8. Each point represents a fit to 300 random selections of that number of bursts, with the error bars representing the standard deviation of all of the fitted peaks. Our findings show the expected effect that as more bursts are included in a sample from a constant-length observation, the average time between bursts will decrease along with the fitted wait-time distribution peak. We find that the distribution of fitted wait times peaks exponentially decays with added bursts with a timescale of ~ 29 seconds. We observe the same effect in the Zhang et al. (2018) dataset, which shows a timescale of ~ 25.5 seconds. The peak obtained by Gourdji et al. (2019) using this data is shown in the figure and matches with our fitted exponential curve. We perform a similar analysis by filtering out the lowest fluence bursts from our sample and find that the wait time peak increases as the minimum fluence limit is increased, and weaker bursts are excluded. This serves to explain the higher wait-time peaks calculated by previous papers with fewer bursts and higher fluence limits.

5.3. Short-period periodicity search

In this section we discuss the results of various periodicity searches tested on this burst sample to search for a short-period periodicity (millisecond to hundreds of seconds).

5.3.1. Difference Search

We first perform a periodicity search on the burst times (μ_t in Table 2) by calculating the differences between consecutive pulse times and searching over a range of trial periods to determine how many differences are evenly divisible, within some tolerance, by this period. We searched over trial periods starting with the minimum difference between pulses, in integer divisors down to the minimum difference divided by 256, after removing all differences less than 50 ms, in both the full set of pulses and 100 trials where only three-quarters of the bursts were randomly selected (to sample a more complete range of minimum differences). We searched tolerances ranging from 1% to 50%. We also searched 1000 simulated time series of identical length, with the same number of pulses distributed randomly, using the same methodology in order to gauge the significance of any detected periodicities. Above a 50% tolerance, we get many more pulse matches in all of the random time-series than we do with the real data, likely due to the FRB pulse distribution not following a random distribution (see Figure 8 for the distribution of pulse arrival time differences).

The most significant period found was 658.838 milliseconds, which fit nine pulses at a tolerance of 3%, with a false alarm probability of 0.3% for random trials

¹¹ Table 2, accessible at <https://doi.org/10.3847/1538-4357/aadf31>

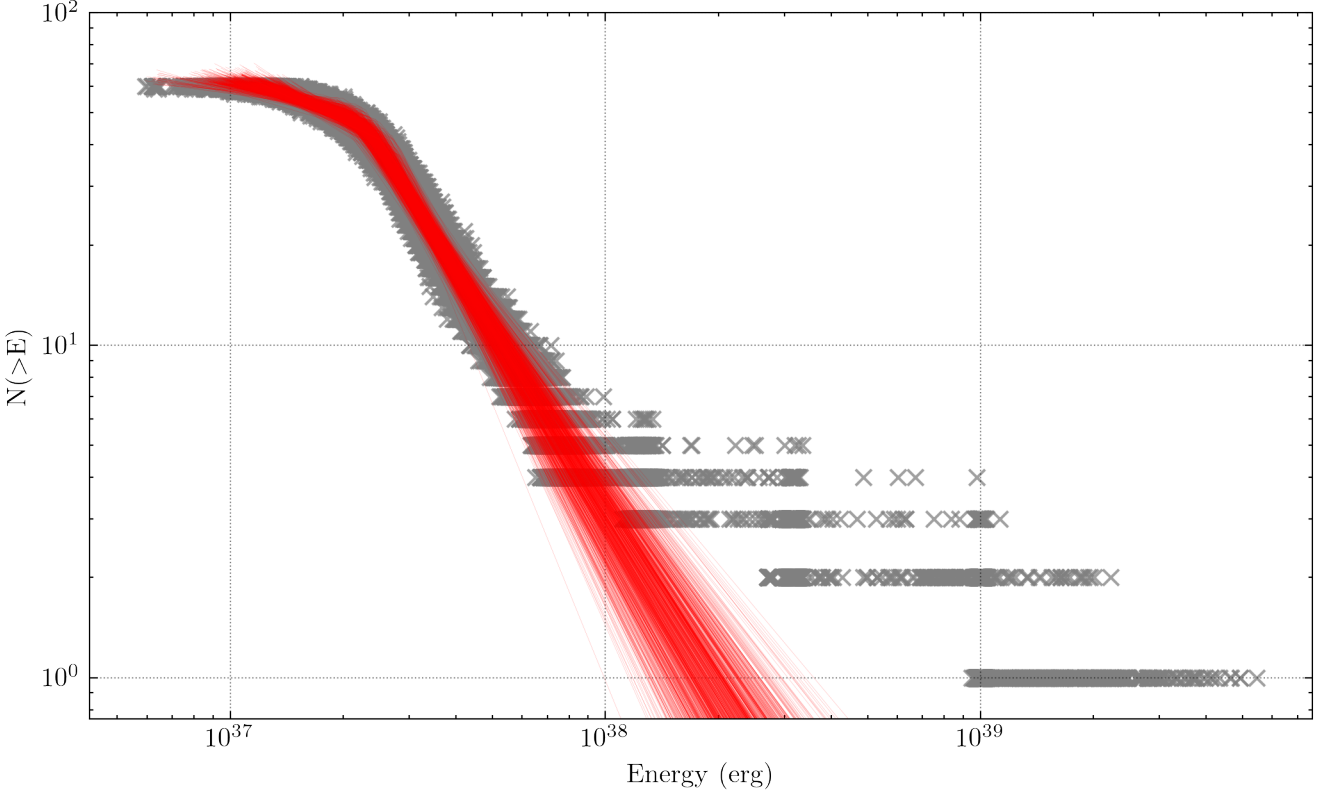


Figure 7. Cumulative energy distribution of bursts above our completeness limit of 5.81×10^{36} ergs. The grey points show the cumulative energy distributions created by bootstrapping the burst energies. The red lines show the broken power-law fit to each of these cumulative energy distributions. See Section 5.1 for more details.

at that tolerance. However, considering all 50 tolerance values searched over two observations, the effective FAP is 30%, and we therefore conclude that no periodicity can be detected through this differencing method.

5.3.2. Fast Folding Algorithm

We ran a fast folding algorithm (FFA) on each observation using `riptide` (Morello et al. 2020). The FFA folds each dedispersed times series over a range of trial periods to create an integrated pulse profile. For each observation, we searched time series with DMs ranging from 550 pc cm^{-3} to 580 pc cm^{-3} and at periods greater than 500 ms (the approximate period at which folding algorithms are more sensitive than Fourier techniques; see Parent et al. 2018) and less than 20 s (to ensure a sufficient number of pulses across the observation for a pulsed detection). We used 1024 output bins, with boxcar filters providing sensitivity to pulses with widths ranging from 1 to 300 ms.

First, candidates due to RFI, such as periods at exact integers and known RFI frequencies, were removed. Of the remaining candidates, a signal-to-noise cutoff of 10σ was applied for a total of 1,250 candidate periods between the two observations.

We then folded the relevant dedispersed time series for each candidate using the `prepfold` command from the PRESTO (Ransom 2011) package at the candidate period and DM identified by `riptide`. We allowed `prepfold` to search in DM in order to determine which candidates had signal-to-noise ratios which peaked for DMs inside of the searched range. We expanded our acceptable DM range from 520 to 610 pc cm $^{-3}$ to allow leeway in `prepfold`'s search, leaving 91 periodic candidates in total. We visually inspected these profiles and found that all were consistent with RFI or noise, with no evidence of emission at the same phase over time or frequency. We compared the candidate periods found by the algorithm on both observations, and found that the only common periods were caused by RFI.

5.3.3. `frbpa`

We used `frbpa` (Aggarwal et al. 2020) to search for a short-period periodicity using the burst times (MJDs). We used two methods: search to find the period that minimizes the fractional width of folded profile (Rajwade et al. 2020b) and a Quadratic-Mutual-Information-based periodicity search technique (Huijse et al. 2018). In the first method, we phase-coherently folded the burst times between trial periods and gen-

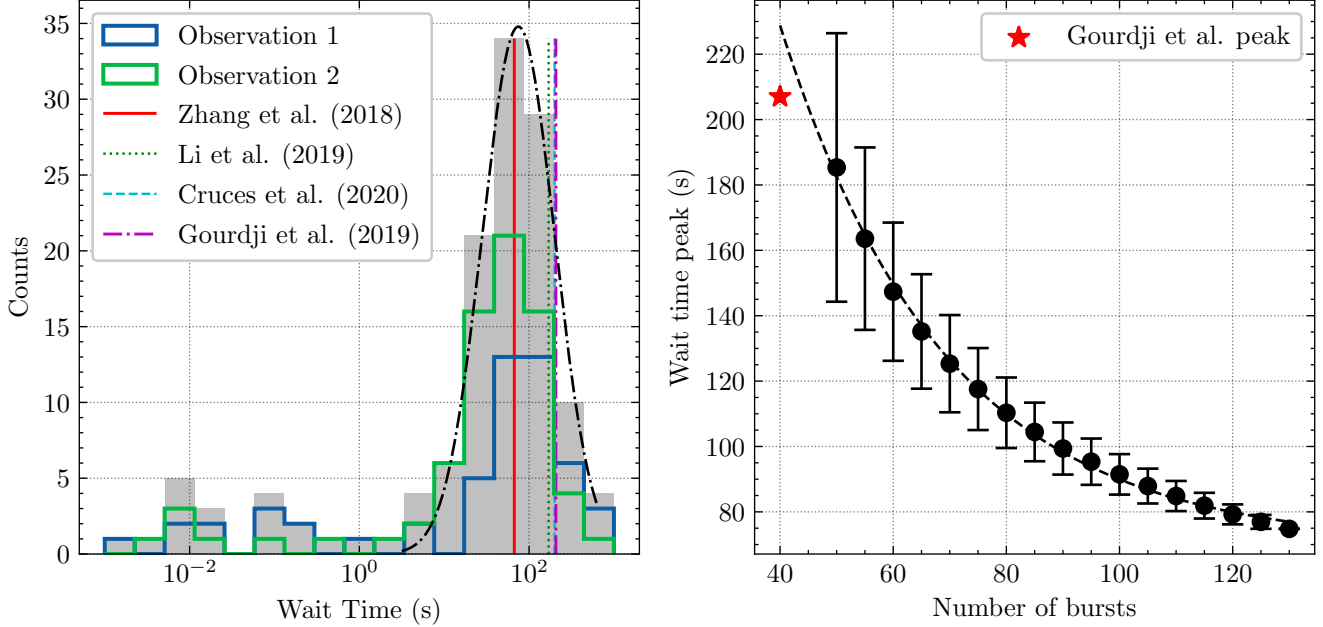


Figure 8. Left: the cumulative wait time distribution for both observations is plotted in gray, with the fitted log-normal function peaking at 74.8 ± 0.1 s. The individual observations are plotted in green and blue, respectively. The fitted wait-time peaks from previous works are noted with vertical lines. Right: the average fitted wait-time peaks as a function of the number of bursts randomly selected from the full sample. The fitted exponential distribution is shown with a black dashed line, and the error bars represent one standard deviation of the fitted peaks. The fitted peak from Gourdji et al. (2019) is represented with a red star.

erated a set of profiles consisting of the source activity with respect to the trial period phase. We then measured the width of the source activity in each folded profile. Low width would indicate that source activity is concentrated in a small set of contiguous phase windows, indicating the presence of periodic activity (Rajwade et al. 2020b). The second method uses quasi-mutual-information to estimate the period. It has been shown to be robust to noise and works well on sparsely sampled data as well (Huijse et al. 2018). We searched for periods between 1–1000 seconds on bursts from the two days individually and did not recover any significant period.

5.3.4. Lomb-Scargle

We also used `timeseries.LombScargle` from the `astropy` library (Astropy Collaboration et al. 2013; Price-Whelan et al. 2018) to search for periods ranging from 100 ms to 1000 seconds on the bursts from the two observations separately. Note that sensitivity to 100-ms periods requires sampling frequencies higher than the traditional Nyquist limit. This is possible because the effective Nyquist frequency for unevenly sampled data set is much smaller than the traditional limit (VanderPlas 2018). The most significant periods are approximately 118 and 179 milliseconds. However, false alarm probabilities of around 3% and 26%, respectively, in-

dicate that the detected periods are unlikely to be real. We therefore we conclude that we did not detect any significant periodicity in the bursts using the Lomb-Scargle method.

5.4. Burst Rate

Previous observations of FRB 121102 have found significant evidence for pulse clustering on short time scales, where the burst separations deviate from a Poissonian distribution (Oppermann et al. 2018; Oostrum et al. 2020; Cruces et al. 2020). The Weibull distribution, as described in Oppermann et al. (2018), is a modification of the Poisson distribution, with a shape parameter k describing the degree of pulse clustering. Clustering is present for $k < 1$ with lower values corresponding to more clustering, while $k = 1$ reduces to the Poissonian case; a value of $k \gg 1$ causes the distribution to peak more sharply at the event rate and indicates a periodic signal. A better understanding of the burst statistics may help us understand the progenitor of FRB 121102 and help strategize the timing of future observations.

Figure 9 shows the cumulative probability density of the wait times between consecutive bursts, fitted to the Weibull and Poisson cumulative density functions as defined by Oppermann et al. (2018). The fitted values are given in Table 4. In Figure 9, we also plot the values

of the reduced chi-squared statistic for the Poisson and Weibull distributions when fitted to only the wait times longer than a range of chosen minimum wait times. We observe that both the Poisson and Weibull distributions fit the main population of longer wait times much better than the entire set of bursts. The Weibull distribution's ability to account for clustering allows it to have a significantly better fit when including shorter wait times, but it is only slightly favored over the Poisson distribution when fitting only longer wait times. We find that the reduced chi-squared statistic is less than one for the Weibull fit to wait times greater than one second, indicating that the distribution is overfitted. These findings may indicate that the main distribution of bursts with longer wait times roughly follows a Poissonian distribution, while the entire burst rate distribution cannot be accurately described with solely a Poisson or Weibull distribution. This may result from our decision to consider each burst as a separate burst rather than a sub-component of a broad burst.

In addition to their observations, [Cruces et al. \(2020\)](#) used the original dataset from [Gourdji et al. \(2019\)](#) to study the burst rate statistics and found that the addition or removal of the sub-second wait time population in each dataset significantly impacts the extrapolated burst rate behavior. In each case, removing these short wait times led to the fitted Weibull shape parameter k increasing towards one, further indicating that the main distribution of pulses may follow a Poissonian distribution while the shorter distributions do not. However, the sample used in [Cruces et al. \(2020\)](#) only had two sub-second wait times; our more extensive sample of short wait times allows us to confirm this behavior with more statistical significance. Using our fits across various minimum wait time cutoffs, we find that the fitted shape parameter k increases with the minimum wait time, reaching a value of $k = 1$ at a minimum wait time cutoff of roughly 0.1 s.

Table 4. Fitted burst rate distributions

	Rate (hour ⁻¹)	k	χ^2	r^2
Poisson (all)	65 ± 8.4	...	495	0.953
Weibull (all)	42 ± 9	0.63 ± 0.07	27.5	0.970
Poisson ($\delta t > 1$ s)	41 ± 1.6	...	1.076	0.994
Weibull ($\delta t > 1$ s)	46 ± 1.5	1.16 ± 0.04	0.368	0.997

NOTE—The posterior values for the Poisson and Weibull distributions as well as the reduced chi-squared statistic and r^2 value, fit both to the entire set of wait times as well as only wait times greater than one second. The errors represent 1σ uncertainties.

5.5. Implications for progenitor models

Based on our results, any progenitor model proposed for FRB 121102 would have to explain the following observations: (1) band-limited emission; (2) varying peak emission of the spectra and its lack below 1300MHz; (3) median scattering timescale of 0.7 ms, with a maximum value of around 2 ms; (4) rapid variability of these three properties at second timescales. Further, some of these observations have also been reported for other FRBs ([Kumar et al. 2021](#); [Shannon et al. 2018](#); [Pastor-Marazuela et al. 2020](#)).

The narrow spectral width or band limited emission is very similar to the frequency structure reported recently for giant pulses from two young pulsars: Crab (PSR B0531+21) and PSR J0540–6919 ([Bij et al. 2021](#); [Thulasiram & Lin 2021](#); [Geyer et al. 2021](#)). As noted by [Geyer et al. \(2021\)](#), the environment of FRB 121102 (star-forming region, continuum radio source) is indicative of a supernova remnant or a pulsar wind nebula that suggests a possible relation between FRBs and young energetic pulsars like PSR J0540–6919. The band limited emission of PSR J0540–6919 is possibly intrinsic ([Geyer et al. 2021](#)), while both intrinsic as well as propagation models have been suggested to explain the band-limited emission of repeating FRBs ([Cordes et al. 2017](#); [Metzger et al. 2019](#); [Simard & Ravi 2020](#)).

One such intrinsic emission model for FRBs is the synchrotron maser emission model, produced by flare ejecta from a young magnetar ([Metzger et al. 2019](#)). Although, this model can explain the band-limited emission of repeating FRBs, the predicted emission width $\Delta\nu/\nu \sim 1$ is much larger than what we observe ($\Delta\nu/\nu \sim 240/1400 \sim 0.17$) in our burst sample. Another possibility is that the spectral structure is caused by plasma lensing near FRB 121102 ([Cordes et al. 2017](#)). Lensing can produce strong magnifications along with multiple burst images on short timescales (μ s to tens of ms). This model can also explain the short timescale variation in DM observed in our sample (see Figure 6).

5.6. Comparison to previous work

In this work, we have presented 93 additional bursts detected on reprocessing the data presented in [Gourdji et al. \(2019\)](#). All the tools and software used in our pipeline are independent of the ones used in the original work. This brings the critical question of understanding why our pipeline detected more bursts or why the original work missed the bursts. While an exhaustive comparison of the two pipelines using a standard dataset consisting of simulated FRBs is beyond the scope of this work, here, we try to investigate the reasons for different results based on our understanding of the software used.

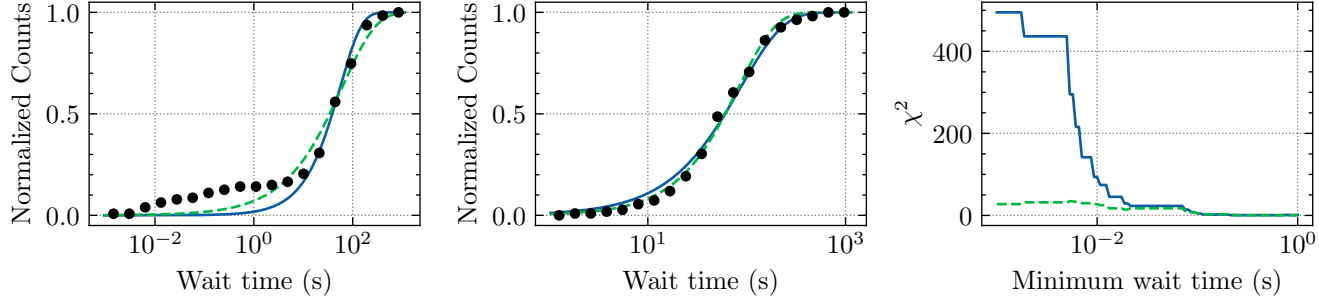


Figure 9. The cumulative wait time distributions fitted by the Poisson (blue solid lines) and Weibull (green dashed lines) distributions for the entire sample of wait times (left) and for the population of wait times greater than one second (middle). The fitted values for the Poisson distribution for the left and middle plots are $r = 65 \text{ hr}^{-1}$ and $r = 41 \text{ hr}^{-1}$ respectively. The fitted values of the Weibull distribution are $k = 0.634$, $r = 42 \text{ hr}^{-1}$ and $k = 1.162$, $r = 46 \text{ hr}^{-1}$ respectively. Right: The chi-squared statistic of the Poisson and Weibull fits, when fitted to wait times greater than the minimum wait time. While the middle and right panels show that both the Weibull and Poisson distributions fit the longer wait times well, the left panel shows that neither distribution accurately fits for the larger sample of sub-second wait times. The right panel shows that pulse clustering starts to impact the fits once wait times shorter than $\sim 50 \text{ ms}$ are considered.

We discuss three reasons that might contribute to very different recovery rates¹² of the two pipelines.

5.6.1. Threshold signal-to-noise ratio

Although Gourdji et al. (2019) used a S/N threshold of 6 for the search, they discarded candidate groups with a maximum S/N less than 8. We used a S/N threshold of 6 in our search. Therefore, they would have missed low S/N candidates.

5.6.2. Single-pulse search software

Gourdji et al. (2019) used `single_pulse_search.py` (Ransom 2011) to search for the bursts, and manually verified the candidates. In contrast, we used HEIMDALL for the single-pulse search, and FETCH for classification. Keane & Petroff (2015) highlight several steps at which a single-pulse search pipeline might miss a transient. Few such steps are sizes of boxcar convolutional kernel, spacing between DM trials, the position of the boxcar convolution with respect to the phase of the pulse, clustering of redundant candidates, etc. Although recovery rates for both these search softwares have been shown to be $>90\%$ in their respective pipelines (Patel et al. 2018; Agarwal et al. 2020b; Gupta et al. 2021), a thorough comparison of the two search strategies has so far not been done.

5.6.3. RFI mitigation and classification

Gourdji et al. (2019) used a different RFI mitigation strategy than our pipeline. They used the classifier (SPS)

presented in Michilli et al. (2018) to filter the RFI candidates and then manually verified the remaining 125 candidates to search for real pulses. SPS was designed specifically to search for Galactic single pulses in a LOFAR survey. Features in LOFAR data would be very different from the data used in this study. This is primarily due to different observing bands (1.4GHz for this study, compared to 100MHz for LOFAR), RFI environment, telescopes, and observing backends. Moreover, the dispersion in FRB pulses is typically much larger than that seen in Galactic transients. Due to these differences, it is not possible to translate the performance of SPS on LOFAR data to the data used in this work. Michilli et al. (2018) mention the use of specially designed filters for such datasets on which SPS was not trained, but they did not report the performance of these filters on any such data. Agarwal et al. (2020a) and Connor & van Leeuwen (2018) also highlight that it is non-trivial to generalize a machine learning algorithm to unseen data without rigorous pre-processing and injection tests. It is therefore possible that SPS missed to correctly identify real pulses that were correctly detected by `single_pulse_search.py`.

As mentioned previously, we used spectral kurtosis for RFI mitigation (Nita & Gary 2010) and used FETCH for classification. It is known that very strict RFI flagging can lead to a reduced recovery rate, as the RFI algorithm might flag real signal as RFI (Rajwade et al. 2020a). Spectral kurtosis is robust to astrophysical signals and performs better than the simple median-based RFI thresholds (Nita & Gary 2010). FETCH was developed to be robust to different telescopes, observing configurations and RFI environments (Agarwal et al. 2020a). We accomplished this by a carefully designed pre-processing and training strategy. We also showed

¹² By recovery rate, we mean the percentage of transients (above the completeness limit) correctly identified by the software. A perfect pipeline would have a recovery rate of 100%, indicating that it can detect all transients present in the data.

that the performance of FETCH remains consistent on unseen data. This has been further established by the new FRBs discovered using FETCH on different telescopes (Kumar et al. 2019; Law et al. 2020; Aggarwal et al. 2020; Rajwade et al. 2020b; Kumar et al. 2021; Pleunis et al. 2021; Kirsten et al. 2021).

5.6.4. General comments

As mentioned in Section 3.3, a robust analysis of any single-pulse search software and pipeline requires exhaustive injection analysis. Such an analysis can highlight the percentage of transients recovered with respect to various physical parameters of interest, like DM, width, phase, etc. These metrics are essential in understanding possible inefficiencies and estimating the completeness of any single-pulse search. Such analysis done for specific pipelines that use HEIMDALL has reported a recovery rate of $> 90\%$ (Agarwal et al. 2020b; Gupta et al. 2021). While our pipeline is not identical, it is very similar to the one reported by Agarwal et al. (2020b). On a less diverse dataset, the recovery rates for `single_pulse_search.py` were also reported to be $> 90\%$ (Patel et al. 2018), but a more rigorous analysis would better assess the robustness of this search software.

Additionally, if a machine learning classifier is deployed in a single-pulse search pipeline, then it is necessary to estimate the recovery rate for the classifier itself. Such rigorous analyses have been performed for some classifiers (Agarwal et al. 2020a; Gupta et al. 2021), and provide insights into their recovery rate estimates. The robustness of a classifier to unseen data should also be carefully investigated (or verified by manual inspection), before reporting the completeness of any search. While human recovery rates for visual classification of thousands of candidates have not been estimated for FRBs, similar estimates are present in computer vision literature. Here, the neural networks (a top-5 error rate of 3.5%) routinely outperform humans (a top-5 error rate of 5.1%) in image classification tasks (He et al. 2015; Russakovsky et al. 2014).

Further, as most of the bursts detected in this sample are narrow-band (i.e., present only in a part of the frequency band), traditional searches might still miss bursts. Sub-banded searches would be more sensitive to detect such band-limited bursts, especially at wide-band systems (R. Anna-Thomas et al. 2021, in preparation; Kumar et al. 2021; Gourdji et al. 2019).

5.7. Caveats

Finally, it is appropriate to highlight and reiterate four main caveats to the analysis presented in this work. (1) The data used in this analysis was downsampled to 64

frequency channels. We did not have access to the native resolution data; therefore, all the search and analysis was performed on downsampled data. The sensitivity of single-pulse search would be higher on native resolution data; therefore, our pipeline may have missed some pulses. (2) We only performed a search on the data that averaged over the full bandwidth to create time-series. Given the band-limited nature of many bursts, a sub-band search on this data might reveal weaker and narrower bursts. (3) As mentioned previously, our estimate of completeness limit is not robust, as such a robust estimate requires injection analysis that was not possible with the available data. (4) The reported properties of the bursts depend on the assumption that burst spectra and profile follow the assumed functional forms used for fitting.

6. CONCLUSIONS

This paper presents a dense sample of FRB 121102 bursts detected at L-band using Arecibo Observatory, analyzed as a part of The Petabyte Project. More importantly, we report 93 new bursts detected with our single-pulse search pipeline, as compared to the published results (Gourdji et al. 2019), making a total of 133 burst detections in 3 hours of data. We have developed a robust burst fitting procedure to model the spectro-temporal properties of FRBs and provide it as a user-friendly python package BURSTFIT¹³. We use the MCMC procedure implemented in BURSTFIT to estimate the properties of all the bursts in our sample. We find that the burst spectra can be well modeled using a Gaussian function, with a median width of 230 MHz and a median peak at 1608 MHz. Most of the burst emission is present in the top of our band, and there is a lack of emission below 1300 MHz, consistent with other published results (Gourdji et al. 2019; Platts et al. 2021). Many bursts also show a scattering tail, with a median timescale of 0.7 ms. Some bursts show complex structures like multiple components and frequency drift. The wait time distribution of the bursts shows two distributions, at millisecond and seconds timescales. The latter of the two follows a log-normal distribution, with the peak at 74.8 s, consistent with other published results (Zhang et al. 2018). We further note that the peak of the wait time changes significantly based on the number of bursts in an observation. We find that both Poisson and Weibull distributions fit the burst rate distributions at long wait times (> 1 second) equally well, and neither accurately describes the whole burst rate distribution.

¹³ <https://github.com/thepetabyteproject/burstfit>

We did not detect any short-period periodicity in the bursts. The cumulative burst energy distribution is well modeled by a double power-law with a break. We find the value of low and high energy slopes to be -0.4 ± 0.1 and -1.8 ± 0.2 with a break at $(2.28 \pm 0.19) \times 10^{37}$ ergs. Our analysis reveals that only the bursts that are completely within the band should be used for energy distribution analysis. We discuss some possible differences between our single-pulse search pipeline and the one used by Gourdji et al. (2019), to explain the different results obtained using the two approaches. All the analysis scripts and results presented in this paper are openly available in a Github repository¹⁴ for the community to use in their repeater burst analyses.

7. ACKNOWLEDGEMENTS

We would like to thank Kelly Gourdji and Jason Hessels for sharing the data. K.A., R.A.T., S.B.S acknowledge support from NSF grant AAG-1714897. S.B.S is a CIFAR Azrieli Global Scholar in the Gravity and the Extreme Universe program. EFL and MAM are supported by NSF AAG award #2009425. This research was made possible by the NASA West Virginia Space Grant Consortium, Grant #80NSSC20M0055. The Arecibo Observatory is a facility of the National Science Foundation operated under cooperative agreement by the University of Central Florida and in alliance with Universidad Ana G. Mendez, and Yang Enterprises, Inc. We are saddened by the extremely tragic collapse of the Arecibo Telescope in December 2020.

APPENDIX

Table 5 shows the fitted properties (with 1σ errors) of all the bursts reported in this analysis.

Table 5. Properties of all the bursts presented in this analysis.

Burst	a	μ_f	σ_f	S	μ_t ^b	σ_t	τ	DM
ID	(MHz)	(MHz)	(MHz)	(Jy ms)	(MJD)	(ms)	(ms)	(pc cm $^{-3}$)
B1*	1560^{+30}_{-30}	210^{+40}_{-40}	$0.09^{+0.02}_{-0.02}$	57644.408906976(1)	$0.0^{+0.02}_{-0.02}$	$1.9^{+0.3}_{-0.3}$	$565.3^{+0.4}_{-0.4}$	
B2*	1200^{+10}_{-10}	50^{+10}_{-10}	$0.043^{+0.007}_{-0.007}$	57644.40956768(1)	$1.35^{+0.05}_{-0.05}$	-	$562.4^{+0.8}_{-0.8}$	
B3.1†	2900^{+300}_{-600}	800^{+300}_{-200}	$0.6^{+0.7}_{-0.3}$	57644.409673699(3)	$0.4^{+0.2}_{-0.2}$	$1.3^{+0.7}_{-0.7}$	$566.8^{+0.8}_{-0.9}$	
B3.2†	1100^{+300}_{-1400}	1000^{+2000}_{-1000}	$0.09^{+0.13}_{-0.04}$	57644.40967384(2)	$0.3^{+1.4}_{-0.2}$	$0.3^{+0.7}_{-0.1}$	$564.7^{+1.5}_{-0.4}$	
B4†	3100^{+200}_{-600}	550^{+80}_{-110}	2^{+4}_{-2}	57644.410072889(4)	$1.1^{+0.2}_{-0.2}$	$0.3^{+0.2}_{-0.1}$	564^{+1}_{-1}	
B5†	2100^{+900}_{-1600}	2700^{+900}_{-1200}	$0.19^{+0.05}_{-0.04}$	57644.410157834(4)	$0.7^{+0.3}_{-0.3}$	$1.0^{+0.4}_{-0.3}$	$562.1^{+0.7}_{-0.6}$	
B6.1	1393^{+7}_{-7}	183^{+7}_{-7}	$0.47^{+0.02}_{-0.03}$	57644.411071954(1)	$1.09^{+0.03}_{-0.04}$	-	$562.3^{+0.2}_{-0.1}$	
B6.2	1417^{+4}_{-5}	102^{+5}_{-4}	$0.33^{+0.03}_{-0.02}$	57644.4110719755(9)	$0.57^{+0.03}_{-0.02}$	-	$560.9^{+0.2}_{-0.1}$	
B7.1†	3100^{+200}_{-300}	430^{+60}_{-80}	10^{+20}_{-10}	57644.412240214(5)	$0.7^{+0.3}_{-0.4}$	$0.8^{+0.4}_{-0.4}$	569^{+3}_{-3}	
B7.2†	1460^{+20}_{-20}	90^{+30}_{-20}	$0.09^{+0.01}_{-0.01}$	57644.41224043(2)	$1.9^{+0.9}_{-1.0}$	$1.2^{+0.6}_{-0.5}$	569^{+3}_{-2}	
B8†	3000^{+200}_{-600}	700^{+100}_{-100}	$1.1^{+1.5}_{-0.7}$	57644.414123628(4)	$1.0^{+0.3}_{-0.3}$	$0.8^{+0.4}_{-0.3}$	$567.5^{+0.9}_{-0.7}$	
B9*	1430^{+10}_{-10}	75^{+9}_{-9}	$0.076^{+0.003}_{-0.003}$	57644.41447161(2)	$2.0^{+0.6}_{-0.6}$	$0.4^{+0.6}_{-0.6}$	564^{+2}_{-2}	
B10	1630^{+10}_{-10}	82^{+8}_{-8}	$0.1^{+0.01}_{-0.01}$	57644.414475391(7)	$1.4^{+0.3}_{-0.3}$	$0.5^{+0.3}_{-0.2}$	562^{+3}_{-3}	
B11	1550^{+10}_{-10}	100^{+10}_{-10}	$0.074^{+0.008}_{-0.007}$	57644.414878803(4)	$0.8^{+0.2}_{-0.2}$	$0.3^{+0.2}_{-0.1}$	$560.3^{+0.9}_{-0.9}$	
B12	3100^{+200}_{-300}	450^{+60}_{-80}	20^{+20}_{-10}	57644.41537809(1)	$1.9^{+0.5}_{-0.5}$	$1.5^{+1.3}_{-0.8}$	569^{+3}_{-4}	
B13	1692^{+13}_{-9}	90^{+20}_{-10}	$0.14^{+0.01}_{-0.01}$	57644.416314736(5)	$1.5^{+0.2}_{-0.2}$	$0.6^{+0.3}_{-0.2}$	572^{+1}_{-1}	
B14	1260^{+10}_{-10}	67^{+9}_{-8}	$0.13^{+0.02}_{-0.02}$	57644.41830674(8)	3^{+1}_{-1}	$1.6^{+0.6}_{-0.5}$	562^{+6}_{-5}	
B15.1†	1550^{+10}_{-10}	80^{+10}_{-10}	$0.07^{+0.01}_{-0.01}$	57644.418309206(7)	$0.9^{+0.3}_{-0.3}$	$0.8^{+0.5}_{-0.4}$	565^{+2}_{-1}	
B15.2†	2000^{+1000}_{-1000}	3000^{+1000}_{-1000}	$0.12^{+0.03}_{-0.04}$	57644.418309273(2)	$0.2^{+0.2}_{-0.1}$	$0.7^{+0.2}_{-0.2}$	$569.4^{+0.4}_{-0.5}$	
B16†	3100^{+200}_{-600}	510^{+60}_{-110}	6^{+9}_{-5}	57644.420508580(4)	$1.2^{+0.2}_{-0.2}$	$0.5^{+0.3}_{-0.2}$	570^{+2}_{-2}	

Table 5 *continued*

¹⁴ <https://github.com/thepebyteproject/FRB121102>

Table 5 (continued)

Burst	<i>a</i>	μ_f	σ_f	<i>S</i>	<i>b</i>	μ_t	σ_t	τ	DM
ID		(MHz)	(MHz)	(Jy ms)		(MJD)	(ms)	(ms)	(pc cm ⁻³)
B17		2000^{+1000}_{-2000}	3000^{+1000}_{-1000}	$0.15^{+0.05}_{-0.04}$	57644.42110545(1)	$1.5^{+0.6}_{-0.5}$	$0.7^{+1.0}_{-0.4}$	570^{+1}_{-2}	
B18*		1530^{+30}_{-30}	140^{+30}_{-30}	$0.046^{+0.008}_{-0.008}$	57644.426303862(4)	$1.5^{+0.1}_{-0.1}$	-	$564.8^{+0.8}_{-0.8}$	
B19*		1330^{+30}_{-30}	160^{+20}_{-20}	$0.11^{+0.02}_{-0.02}$	57644.42721003(2)	$1.9^{+0.8}_{-0.8}$	$1.6^{+0.5}_{-0.5}$	564^{+1}_{-1}	
B20†		2900^{+400}_{-1000}	1000^{+2000}_{-400}	$0.23^{+0.47}_{-0.08}$	57644.427376859(4)	$0.7^{+0.3}_{-0.3}$	$0.6^{+0.5}_{-0.3}$	$565.6^{+0.8}_{-0.6}$	
B21†		3100^{+200}_{-400}	600^{+100}_{-100}	3^{+7}_{-2}	57644.42794036(2)	$4.2^{+0.9}_{-1.0}$	$1.8^{+1.7}_{-0.8}$	576^{+4}_{-5}	
B22†		3000^{+300}_{-700}	700^{+100}_{-200}	$1.3^{+1.7}_{-0.9}$	57644.428593784(8)	$1.9^{+0.4}_{-0.4}$	$1.5^{+0.6}_{-0.6}$	568^{+2}_{-2}	
B23		1699^{+14}_{-9}	70^{+20}_{-10}	$0.089^{+0.009}_{-0.008}$	57644.430170170(2)	$0.7^{+0.1}_{-0.1}$	$0.3^{+0.2}_{-0.1}$	$569.0^{+1.0}_{-1.0}$	
B24*		1670^{+20}_{-20}	80^{+20}_{-20}	$0.0384^{+0.0007}_{-0.0007}$	57644.430170303(1)	$0.02^{+0.05}_{-0.05}$	$1.2^{+0.3}_{-0.3}$	$563.0^{+0.5}_{-0.5}$	
B25		1750^{+1380}_{-70}	200^{+390}_{-60}	$0.16^{+3.67}_{-0.03}$	57644.430171419(4)	$1.4^{+0.2}_{-0.2}$	$0.7^{+0.3}_{-0.3}$	568^{+1}_{-1}	
B26		1470^{+10}_{-10}	110^{+20}_{-10}	$0.096^{+0.009}_{-0.009}$	57644.431295361(4)	$0.8^{+0.2}_{-0.2}$	$0.5^{+0.2}_{-0.2}$	$565.6^{+0.7}_{-0.7}$	
B27		1340^{+70}_{-1400}	1000^{+2000}_{-1000}	$0.17^{+0.11}_{-0.09}$	57644.43223490(2)	$2.0^{+1.0}_{-0.7}$	$1.1^{+0.5}_{-0.4}$	570^{+2}_{-2}	
B28		1750^{+40}_{-20}	100^{+20}_{-10}	$0.14^{+0.03}_{-0.02}$	57644.432242722(1)	$0.59^{+0.05}_{-0.05}$	$0.16^{+0.09}_{-0.05}$	$561.3^{+0.5}_{-0.5}$	
B29		1680^{+1440}_{-30}	130^{+480}_{-40}	$0.06^{+1.5}_{-0.01}$	57644.434045197(4)	$0.6^{+0.2}_{-0.2}$	$0.4^{+0.4}_{-0.2}$	562^{+1}_{-3}	
B30		1440^{+10}_{-10}	100^{+20}_{-10}	$0.12^{+0.01}_{-0.01}$	57644.43636575(2)	$2.1^{+0.6}_{-0.5}$	$1.2^{+0.5}_{-0.4}$	568^{+2}_{-3}	
B31		1502^{+6}_{-6}	100^{+8}_{-7}	$0.19^{+0.01}_{-0.01}$	57644.438794966(4)	$1.6^{+0.1}_{-0.2}$	$0.5^{+0.1}_{-0.1}$	$566.6^{+0.7}_{-0.7}$	
B32		1410^{+8}_{-8}	79^{+9}_{-8}	$0.14^{+0.01}_{-0.01}$	57644.43884518(1)	$1.7^{+0.3}_{-0.4}$	$0.6^{+0.4}_{-0.3}$	564^{+1}_{-1}	
B33		1480^{+20}_{-20}	120^{+20}_{-20}	$0.08^{+0.01}_{-0.01}$	57644.439212855(8)	$1.2^{+0.3}_{-0.4}$	$0.6^{+0.6}_{-0.3}$	$563.0^{+1.0}_{-1.0}$	
B34†		2600^{+600}_{-1400}	2000^{+1000}_{-1000}	$0.27^{+0.1}_{-0.06}$	57644.440688613(5)	$1.3^{+0.4}_{-0.4}$	$1.0^{+0.4}_{-0.3}$	$567.0^{+0.8}_{-0.9}$	
B35		1707^{+5}_{-5}	61^{+6}_{-5}	$0.24^{+0.01}_{-0.01}$	57644.442997729(6)	$2.8^{+0.2}_{-0.2}$	$0.7^{+0.4}_{-0.2}$	575^{+3}_{-3}	
B36†		3100^{+200}_{-400}	470^{+70}_{-90}	10^{+20}_{-10}	57644.44358918(2)	3^{+2}_{-1}	2^{+2}_{-1}	574^{+11}_{-6}	
B37		1410^{+20}_{-20}	130^{+30}_{-20}	$0.065^{+0.007}_{-0.008}$	57644.443590029(3)	$0.58^{+0.11}_{-0.09}$	$0.14^{+0.1}_{-0.04}$	$562.8^{+0.5}_{-0.4}$	
B38		1620^{+20}_{-20}	110^{+20}_{-20}	$0.1^{+0.01}_{-0.01}$	57644.445225058(7)	$0.9^{+0.5}_{-0.5}$	$1.9^{+0.7}_{-0.9}$	567^{+2}_{-2}	
B39		1500^{+10}_{-20}	130^{+10}_{-10}	$0.057^{+0.01}_{-0.006}$	57644.446788124(1)	$0.21^{+0.04}_{-0.04}$	$0.12^{+0.13}_{-0.05}$	$560.9^{+0.1}_{-0.2}$	
B40		1590^{+10}_{-10}	81^{+11}_{-9}	$0.12^{+0.02}_{-0.02}$	57644.447567822(8)	$1.1^{+0.5}_{-0.4}$	$2.0^{+0.8}_{-0.7}$	560^{+3}_{-3}	
B41*		1379^{+1}_{-1}	31^{+1}_{-1}	$0.4^{+0.02}_{-0.02}$	57644.44772750(2)	$0.8^{+0.2}_{-0.2}$	$3.0^{+0.2}_{-0.2}$	559^{+2}_{-2}	
B42		1670^{+10}_{-10}	110^{+20}_{-20}	$0.099^{+0.009}_{-0.008}$	57644.449915568(3)	$0.9^{+0.2}_{-0.2}$	$0.4^{+0.2}_{-0.2}$	$566.0^{+0.8}_{-0.7}$	
B43		1683^{+12}_{-9}	120^{+20}_{-10}	$0.22^{+0.01}_{-0.01}$	57644.451605444(1)	$0.79^{+0.1}_{-0.09}$	$0.9^{+0.1}_{-0.1}$	$568.2^{+0.5}_{-0.5}$	
B44†		3100^{+200}_{-400}	520^{+50}_{-70}	11^{+13}_{-7}	57644.452389712(6)	$1.8^{+0.3}_{-0.3}$	$1.1^{+0.5}_{-0.5}$	569^{+2}_{-4}	
B45		1710^{+1490}_{-60}	160^{+470}_{-70}	$0.07^{+1.81}_{-0.02}$	57644.453937473(4)	$0.9^{+0.2}_{-0.4}$	$0.5^{+0.4}_{-0.2}$	562^{+1}_{-1}	
B46		1371^{+2}_{-2}	61^{+2}_{-2}	$0.41^{+0.01}_{-0.01}$	57644.454477404(8)	$2.8^{+0.2}_{-0.2}$	$0.6^{+0.1}_{-0.1}$	$569.6^{+0.8}_{-0.8}$	
B47		900^{+800}_{-1100}	2000^{+1000}_{-2000}	$0.15^{+0.04}_{-0.09}$	57644.457883227(3)	$0.5^{+0.1}_{-0.1}$	$0.23^{+0.14}_{-0.09}$	$561.9^{+0.3}_{-0.2}$	
B48.1†		2900^{+300}_{-1200}	600^{+2500}_{-100}	1^{+15}_{-1}	57644.464507488(7)	$0.4^{+0.4}_{-0.3}$	$0.7^{+0.6}_{-0.3}$	565^{+4}_{-2}	
B48.2†		0^{+1300}_{-500}	500^{+500}_{-400}	$0.7^{+26.2}_{-0.6}$	57644.4645075(2)	$0.9^{+3.2}_{-0.6}$	$0.7^{+3.6}_{-0.4}$	600^{+100}_{-200}	
B49.1		1660^{+10}_{-10}	140^{+20}_{-10}	$0.49^{+0.03}_{-0.03}$	57644.46475893(1)	$8.3^{+0.5}_{-0.5}$	$2.0^{+0.7}_{-0.6}$	568^{+4}_{-4}	
B49.2		2400^{+700}_{-1400}	2000^{+1000}_{-1000}	$0.16^{+0.05}_{-0.04}$	57644.464759903(1)	$0.2^{+0.1}_{-0.1}$	$0.6^{+0.2}_{-0.1}$	$561.3^{+0.3}_{-0.2}$	
B50		1460^{+10}_{-10}	90^{+10}_{-10}	$0.13^{+0.02}_{-0.01}$	57644.46476275(1)	$1.3^{+1.0}_{-0.9}$	$1.7^{+0.6}_{-0.8}$	561^{+2}_{-2}	
B51†		2500^{+600}_{-900}	1000^{+1000}_{-700}	$0.3^{+0.2}_{-0.2}$	57644.465729923(7)	$1.4^{+0.6}_{-0.4}$	$1.2^{+0.5}_{-0.4}$	569^{+1}_{-1}	
B52		1667^{+5}_{-4}	73^{+6}_{-5}	$0.185^{+0.009}_{-0.009}$	57644.466222289(4)	$1.4^{+0.2}_{-0.2}$	$0.6^{+0.2}_{-0.2}$	570^{+1}_{-1}	
B53		1720^{+30}_{-20}	120^{+30}_{-20}	$0.19^{+0.03}_{-0.02}$	57644.468095365(4)	$1.5^{+0.2}_{-0.2}$	$1.1^{+0.3}_{-0.3}$	572^{+1}_{-1}	
B54*		1600^{+600}_{-600}	100^{+100}_{-100}	$0.0^{+0.1}_{-0.1}$	57644.47117767(7)	0^{+10}_{-10}	$0.9^{+0.2}_{-0.2}$	560^{+40}_{-40}	
B55		1650^{+10}_{-10}	100^{+10}_{-10}	$0.13^{+0.01}_{-0.01}$	57644.474717918(6)	$1.4^{+0.3}_{-0.2}$	$1.3^{+0.5}_{-0.5}$	570^{+2}_{-2}	
B56		1706^{+4}_{-4}	54^{+6}_{-5}	$0.16^{+0.01}_{-0.01}$	57644.477082041(3)	$0.9^{+0.2}_{-0.1}$	$0.9^{+0.2}_{-0.2}$	560^{+2}_{-2}	
B57		1530^{+6}_{-6}	186^{+6}_{-6}	$0.254^{+0.006}_{-0.005}$	57645.4110889611(4)	$0.48^{+0.03}_{-0.02}$	$0.21^{+0.02}_{-0.02}$	$561.75^{+0.06}_{-0.06}$	
B58		1462^{+6}_{-6}	78^{+6}_{-5}	$0.129^{+0.008}_{-0.008}$	57645.411651653(4)	$0.9^{+0.1}_{-0.1}$	$0.4^{+0.1}_{-0.1}$	$564.4^{+0.6}_{-0.7}$	
B59		1537^{+5}_{-4}	68^{+4}_{-4}	$0.2^{+0.01}_{-0.01}$	57645.411889086(9)	$2.2^{+0.4}_{-0.3}$	$1.1^{+0.3}_{-0.3}$	568^{+2}_{-2}	

Table 5 continued

Table 5 (continued)

Burst	<i>a</i>	μ_f	σ_f	<i>S</i>	<i>b</i>	μ_t	σ_t	τ	DM
ID		(MHz)	(MHz)	(Jy ms)		(MJD)	(ms)	(ms)	(pc cm $^{-3}$)
B60.1		3000^{+300}_{-1000}	440^{+80}_{-220}	4^{+6}_{-4}		57645.412281872(4)	$0.8^{+0.2}_{-0.1}$	$0.3^{+0.3}_{-0.2}$	566^{+2}_{-2}
B60.2		2300^{+900}_{-600}	500^{+300}_{-300}	$0.4^{+1.6}_{-0.2}$		57645.412281990(6)	$0.9^{+0.6}_{-0.5}$	$2.5^{+0.6}_{-0.5}$	561^{+2}_{-2}
B61†		1000^{+1000}_{-1000}	2800^{+900}_{-1100}	$0.25^{+0.08}_{-0.07}$		57645.41286869(2)	$2.0^{+2.0}_{-1.0}$	2^{+2}_{-1}	580^{+3}_{-13}
B62		1570^{+10}_{-10}	110^{+10}_{-10}	$0.12^{+0.01}_{-0.009}$		57645.413644740(5)	$1.3^{+0.2}_{-0.2}$	$0.6^{+0.3}_{-0.2}$	567^{+1}_{-1}
B63		1280^{+10}_{-10}	86^{+11}_{-9}	$0.1^{+0.01}_{-0.01}$		57645.41609534(1)	$0.8^{+0.2}_{-0.2}$	$0.6^{+0.2}_{-0.1}$	$562.0^{+0.8}_{-0.9}$
B64†		2000^{+1000}_{-1000}	3000^{+1000}_{-1000}	$0.32^{+0.09}_{-0.09}$		57645.41639521(1)	$1.4^{+0.5}_{-0.5}$	3^{+1}_{-1}	564^{+3}_{-2}
B65		1550^{+10}_{-10}	110^{+20}_{-10}	$0.091^{+0.009}_{-0.009}$		57645.416564818(6)	$1.2^{+0.2}_{-0.2}$	$0.6^{+0.3}_{-0.2}$	$566.0^{+1.0}_{-1.0}$
B66		1440^{+10}_{-10}	120^{+10}_{-10}	$0.105^{+0.009}_{-0.008}$		57645.417467306(6)	$1.6^{+0.2}_{-0.2}$	-	$567.7^{+0.7}_{-0.7}$
B67		1640^{+30}_{-20}	180^{+30}_{-30}	$0.099^{+0.009}_{-0.008}$		57645.417897463(2)	$0.8^{+0.1}_{-0.1}$	$0.3^{+0.1}_{-0.1}$	$564.8^{+0.5}_{-0.5}$
B68†		2000^{+1000}_{-1000}	2000^{+1000}_{-1000}	$0.2^{+0.05}_{-0.06}$		57645.419005902(8)	$1.0^{+0.6}_{-0.5}$	$0.9^{+0.4}_{-0.4}$	$567.9^{+0.9}_{-1.3}$
B69		1450^{+20}_{-10}	80^{+10}_{-10}	$0.059^{+0.009}_{-0.009}$		57645.41920745(1)	$0.7^{+0.3}_{-0.3}$	$0.5^{+0.3}_{-0.2}$	564^{+1}_{-1}
B70†		3100^{+200}_{-500}	600^{+100}_{-100}	$0.9^{+1.7}_{-0.6}$		57645.419896226(4)	$0.8^{+0.3}_{-0.3}$	$0.8^{+0.4}_{-0.3}$	564^{+1}_{-1}
B71		1378^{+5}_{-4}	78^{+5}_{-4}	$0.34^{+0.02}_{-0.02}$		57645.420265931(9)	$1.0^{+0.2}_{-0.2}$	$2.6^{+0.2}_{-0.2}$	$561.1^{+0.9}_{-1.0}$
B72†		3100^{+200}_{-500}	700^{+200}_{-100}	$1.2^{+3.4}_{-0.8}$		57645.420600439(9)	$1.2^{+0.7}_{-0.8}$	2^{+1}_{-1}	559^{+2}_{-2}
B73†		3100^{+200}_{-500}	600^{+100}_{-100}	2^{+3}_{-1}		57645.420679524(7)	$1.5^{+0.6}_{-0.8}$	$1.7^{+0.8}_{-0.7}$	575^{+3}_{-3}
B74†		3100^{+200}_{-400}	520^{+100}_{-90}	5^{+12}_{-4}		57645.420752363(6)	$1.2^{+0.8}_{-0.6}$	$1.9^{+0.7}_{-0.9}$	551^{+11}_{-12}
B75†		2200^{+800}_{-1400}	2700^{+900}_{-1200}	$0.39^{+0.07}_{-0.08}$		57645.421284056(4)	$0.9^{+0.3}_{-0.3}$	$1.8^{+0.3}_{-0.3}$	$567.6^{+0.9}_{-0.7}$
B76		1410^{+10}_{-350}	90^{+20}_{-10}	$0.05^{+0.111}_{-0.006}$		57645.421290699(5)	$0.42^{+0.25}_{-0.09}$	$0.14^{+0.42}_{-0.05}$	$561.6^{+0.6}_{-0.5}$
B77		1312^{+5}_{-5}	51^{+6}_{-6}	$0.12^{+0.01}_{-0.01}$		57645.42161300(2)	$1.3^{+0.5}_{-0.5}$	$0.7^{+0.2}_{-0.2}$	566^{+2}_{-2}
B78		1170^{+20}_{-40}	80^{+40}_{-10}	$0.11^{+0.03}_{-0.02}$		57645.42184846(1)	$0.9^{+0.3}_{-0.2}$	$0.28^{+0.14}_{-0.08}$	$562.4^{+0.7}_{-0.9}$
B79		1702^{+4}_{-4}	57^{+6}_{-5}	$0.18^{+0.01}_{-0.01}$		57645.421872443(3)	$1.2^{+0.2}_{-0.2}$	$1.7^{+0.3}_{-0.3}$	568^{+2}_{-2}
B80		1601^{+7}_{-8}	81^{+8}_{-7}	$0.13^{+0.01}_{-0.01}$		57645.422454976(3)	$0.5^{+0.3}_{-0.2}$	$1.3^{+0.2}_{-0.3}$	$564.4^{+1.0}_{-0.8}$
B81		1720^{+390}_{-10}	60^{+310}_{-20}	$0.05^{+0.1}_{-0.01}$		57645.423009490(6)	$0.78^{+0.08}_{-0.18}$	$0.6^{+0.1}_{-0.2}$	563^{+8}_{-5}
B82†		3100^{+200}_{-400}	580^{+60}_{-70}	4^{+4}_{-2}		57645.424145870(2)	$1.3^{+0.1}_{-0.1}$	-	$569.2^{+0.7}_{-0.7}$
B83†		2400^{+700}_{-1300}	2000^{+2000}_{-1000}	$0.15^{+0.07}_{-0.04}$		57645.424617988(6)	$0.7^{+0.3}_{-0.3}$	$0.4^{+0.2}_{-0.2}$	$564.7^{+0.7}_{-0.5}$
B84†		3000^{+300}_{-700}	600^{+100}_{-200}	1^{+3}_{-1}		57645.425478263(8)	$1.0^{+0.8}_{-0.6}$	$1.7^{+0.9}_{-0.9}$	563^{+2}_{-3}
B85*		1310^{+20}_{-20}	130^{+20}_{-20}	$0.11^{+0.02}_{-0.02}$		57645.426746546(2)	$0.01^{+0.06}_{-0.06}$	$2.0^{+0.4}_{-0.4}$	$566.1^{+0.2}_{-0.2}$
B86		1550^{+10}_{-10}	80^{+10}_{-10}	$0.067^{+0.009}_{-0.008}$		57645.426792398(7)	$0.6^{+0.4}_{-0.3}$	$0.9^{+0.3}_{-0.3}$	563^{+1}_{-1}
B87		1760^{+440}_{-50}	190^{+200}_{-50}	$0.2^{+0.38}_{-0.03}$		57645.426922532(4)	$1.4^{+0.2}_{-0.2}$	$0.9^{+0.3}_{-0.3}$	$571.1^{+0.9}_{-0.9}$
B88.1		2000^{+1000}_{-1000}	2000^{+1000}_{-2000}	$0.17^{+0.06}_{-0.06}$		57645.427338932(7)	$0.7^{+0.4}_{-0.3}$	$1.0^{+0.7}_{-0.5}$	561^{+2}_{-4}
B88.2		1460^{+20}_{-10}	130^{+20}_{-20}	$0.11^{+0.01}_{-0.01}$		57645.427339178(9)	$2.4^{+0.4}_{-0.3}$	-	561^{+1}_{-2}
B89		1479^{+8}_{-8}	120^{+8}_{-7}	$0.18^{+0.01}_{-0.01}$		57645.428904793(6)	$2.4^{+0.2}_{-0.2}$	-	$569.0^{+0.7}_{-0.8}$
B90		1420^{+40}_{-500}	120^{+2790}_{-30}	$0.09^{+0.11}_{-0.02}$		57645.42990044(2)	$2.4^{+0.6}_{-0.6}$	$0.8^{+0.6}_{-0.3}$	565^{+2}_{-2}
B91		1476^{+9}_{-9}	81^{+10}_{-8}	$0.12^{+0.01}_{-0.01}$		57645.43034452(2)	$3.1^{+0.4}_{-0.4}$	-	572^{+2}_{-2}
B92		1721^{+4}_{-4}	39^{+6}_{-4}	$0.17^{+0.02}_{-0.02}$		57645.43044763(1)	$2.6^{+0.8}_{-0.7}$	3^{+1}_{-1}	580^{+10}_{-10}
B93.1		1591^{+9}_{-9}	106^{+10}_{-9}	$0.126^{+0.008}_{-0.008}$		57645.430622487(3)	$1.2^{+0.1}_{-0.2}$	$0.4^{+0.2}_{-0.2}$	$565.3^{+0.8}_{-0.9}$
B93.2		1620^{+10}_{-10}	120^{+20}_{-20}	$0.13^{+0.01}_{-0.01}$		57645.430622591(7)	$1.7^{+0.3}_{-0.3}$	$0.8^{+0.4}_{-0.3}$	564^{+2}_{-2}
B94†		3100^{+200}_{-600}	500^{+60}_{-120}	7^{+10}_{-6}		57645.431306274(4)	$1.1^{+0.2}_{-0.2}$	$0.6^{+0.4}_{-0.3}$	565^{+2}_{-4}
B95		1693^{+11}_{-8}	90^{+20}_{-10}	$0.095^{+0.007}_{-0.007}$		57645.431478373(2)	$0.69^{+0.08}_{-0.08}$	$0.22^{+0.12}_{-0.08}$	$563.5^{+0.6}_{-0.5}$
B96†		2000^{+1000}_{-2000}	2800^{+800}_{-1100}	$0.2^{+0.06}_{-0.05}$		57645.43254531(2)	$2.1^{+0.8}_{-0.9}$	$0.9^{+0.6}_{-0.3}$	565^{+2}_{-1}
B97†		2900^{+400}_{-800}	800^{+500}_{-200}	$0.3^{+0.4}_{-0.1}$		57645.433086695(3)	$0.6^{+0.4}_{-0.4}$	$1.0^{+0.4}_{-0.4}$	$562.4^{+0.9}_{-0.5}$
B98		1667^{+7}_{-7}	67^{+8}_{-7}	$0.094^{+0.01}_{-0.009}$		57645.434330453(5)	$1.1^{+0.2}_{-0.2}$	$0.7^{+0.3}_{-0.3}$	559^{+2}_{-2}
B99†		2000^{+1000}_{-2000}	2800^{+800}_{-1100}	$0.13^{+0.03}_{-0.03}$		57645.440066847(4)	$0.8^{+0.2}_{-0.2}$	$0.3^{+0.2}_{-0.1}$	$565.8^{+0.4}_{-0.4}$
B100		1688^{+4}_{-4}	62^{+5}_{-5}	$0.154^{+0.008}_{-0.007}$		57645.440814641(2)	$1.0^{+0.1}_{-0.1}$	$0.5^{+0.2}_{-0.2}$	$567.0^{+1.0}_{-1.0}$
B101*		1510^{+20}_{-20}	130^{+20}_{-20}	$0.042^{+0.006}_{-0.006}$		57645.441999925(3)	$0.87^{+0.02}_{-0.02}$	-	$568.6^{+0.4}_{-0.4}$

Table 5 continued

Table 5 (continued)

Burst	^a ID	μ_f (MHz)	σ_f (MHz)	S (Jy ms)	μ_t (MJD)	^b σ_t (ms)	τ (ms)	DM (pc cm ⁻³)
	B102	2000^{+1200}_{-300}	300^{+300}_{-200}	$0.2^{+2.7}_{-0.1}$	57645.442100164(8)	$2.1^{+0.4}_{-0.4}$	$0.8^{+0.6}_{-0.4}$	564^{+2}_{-2}
	B103	1470^{+10}_{-10}	90^{+10}_{-10}	$0.08^{+0.01}_{-0.01}$	57645.44263325(1)	$1.4^{+0.3}_{-0.3}$	$0.6^{+0.5}_{-0.3}$	562^{+1}_{-1}
	B104*	1460^{+60}_{-60}	90^{+20}_{-20}	$0.07^{+0.09}_{-0.09}$	57645.4427413(1)	0^{+2}_{-2}	$2.1^{+0.5}_{-0.5}$	569^{+8}_{-8}
	B105	1670^{+10}_{-10}	110^{+20}_{-20}	$0.095^{+0.008}_{-0.007}$	57645.444480955(2)	$0.51^{+0.1}_{-0.09}$	$0.5^{+0.1}_{-0.1}$	$565.4^{+0.5}_{-0.5}$
	B106	1480^{+7}_{-8}	97^{+10}_{-9}	$0.16^{+0.01}_{-0.01}$	57645.444919472(7)	$2.0^{+0.2}_{-0.2}$	$0.5^{+0.2}_{-0.1}$	566^{+1}_{-1}
	B107	2800^{+300}_{-1000}	370^{+70}_{-260}	10^{+10}_{-10}	57645.445443070(5)	$1.2^{+0.3}_{-0.3}$	$0.9^{+0.4}_{-0.4}$	561^{+3}_{-2}
	B108	1488^{+4}_{-4}	83^{+4}_{-4}	$0.141^{+0.006}_{-0.006}$	57645.448802883(2)	$0.66^{+0.03}_{-0.03}$	-	$561.1^{+0.3}_{-0.3}$
	B109	1460^{+5}_{-5}	87^{+5}_{-5}	$0.24^{+0.01}_{-0.01}$	57645.449987035(8)	$2.8^{+0.2}_{-0.2}$	-	568^{+1}_{-1}
	B110*	1620^{+10}_{-10}	100^{+10}_{-10}	$0.1^{+0.01}_{-0.01}$	57645.451201066(8)	$1.7^{+0.4}_{-0.4}$	$1.3^{+0.5}_{-0.5}$	561^{+2}_{-2}
	B111	1469^{+6}_{-6}	58^{+7}_{-6}	$0.109^{+0.01}_{-0.009}$	57645.45198993(1)	$1.6^{+0.2}_{-0.2}$	$0.5^{+0.2}_{-0.1}$	563^{+2}_{-2}
	B112	1442^{+4}_{-5}	68^{+4}_{-4}	$0.142^{+0.008}_{-0.008}$	57645.453426198(4)	$0.59^{+0.08}_{-0.07}$	$0.4^{+0.07}_{-0.06}$	$563.1^{+0.6}_{-0.6}$
	B113	1699^{+4}_{-4}	68^{+6}_{-5}	$0.29^{+0.01}_{-0.01}$	57645.453639067(4)	$2.5^{+0.1}_{-0.2}$	$0.6^{+0.3}_{-0.2}$	569^{+2}_{-2}
	B114	1570^{+20}_{-20}	110^{+20}_{-20}	$0.07^{+0.01}_{-0.01}$	57645.453640216(3)	$0.3^{+0.2}_{-0.1}$	$1.4^{+0.3}_{-0.3}$	$566.5^{+0.7}_{-0.8}$
	B115	1730^{+30}_{-10}	90^{+20}_{-20}	$0.19^{+0.03}_{-0.02}$	57645.454258102(7)	$2.3^{+0.3}_{-0.3}$	$0.9^{+0.6}_{-0.4}$	569^{+3}_{-3}
	B116*	1480^{+40}_{-40}	260^{+60}_{-60}	$0.08^{+0.02}_{-0.02}$	57645.4544929400(9)	$0.05^{+0.07}_{-0.07}$	$1.4^{+0.3}_{-0.3}$	$565.7^{+0.2}_{-0.2}$
	B117	1580^{+20}_{-20}	130^{+30}_{-20}	$0.1^{+0.02}_{-0.01}$	57645.45736147(1)	$1.8^{+0.9}_{-0.8}$	$1.8^{+0.8}_{-0.8}$	563^{+3}_{-3}
	B118	1580^{+30}_{-20}	130^{+30}_{-20}	$0.1^{+0.02}_{-0.01}$	57645.45736147(1)	$1.7^{+0.9}_{-0.8}$	$1.8^{+0.9}_{-0.8}$	563^{+3}_{-3}
	B119	1670^{+60}_{-20}	170^{+60}_{-30}	$0.21^{+0.04}_{-0.02}$	57645.458536220(6)	$1.2^{+0.4}_{-0.3}$	$2.6^{+0.5}_{-0.5}$	569^{+2}_{-2}
	B120	1690^{+1040}_{-30}	130^{+380}_{-30}	$0.09^{+0.87}_{-0.01}$	57645.459103357(6)	$0.8^{+0.3}_{-0.5}$	$1.2^{+0.5}_{-0.4}$	566^{+2}_{-2}
	B121.1	1612^{+2}_{-2}	90^{+2}_{-2}	$0.394^{+0.007}_{-0.007}$	57645.460053270(1)	$0.82^{+0.04}_{-0.04}$	$0.25^{+0.06}_{-0.07}$	$562.1^{+0.2}_{-0.2}$
	B121.2	1321^{+2}_{-3}	178^{+2}_{-2}	$1.73^{+0.02}_{-0.02}$	57645.4600533283(4)	$0.95^{+0.02}_{-0.02}$	$0.36^{+0.02}_{-0.01}$	$561.98^{+0.03}_{-0.03}$
	B121.3	1181^{+9}_{-11}	93^{+9}_{-8}	$0.35^{+0.03}_{-0.02}$	57645.460053409(4)	$1.22^{+0.09}_{-0.07}$	-	$561.6^{+0.2}_{-0.3}$
	B122	1405^{+4}_{-4}	71^{+5}_{-5}	$0.22^{+0.01}_{-0.01}$	57645.462106655(9)	$2.3^{+0.2}_{-0.2}$	$0.5^{+0.2}_{-0.1}$	565^{+1}_{-1}
	B123*	1690^{+20}_{-20}	90^{+20}_{-20}	$0.09^{+0.02}_{-0.02}$	57645.462556118(6)	$1.1^{+0.4}_{-0.4}$	$2.0^{+0.6}_{-0.6}$	567^{+3}_{-3}
	B124	1560^{+10}_{-20}	150^{+20}_{-20}	$0.094^{+0.008}_{-0.008}$	57645.464052738(3)	$1.0^{+0.2}_{-0.2}$	$0.5^{+0.2}_{-0.2}$	$565.3^{+0.5}_{-0.6}$
	B125	1600^{+10}_{-10}	140^{+20}_{-20}	$0.121^{+0.01}_{-0.009}$	57645.464188555(4)	$1.2^{+0.2}_{-0.2}$	$0.7^{+0.2}_{-0.2}$	$564.4^{+0.8}_{-0.8}$
	B126	1600^{+1190}_{-60}	230^{+2380}_{-90}	$0.07^{+0.13}_{-0.02}$	57645.464503855(6)	$0.9^{+0.4}_{-0.5}$	$0.9^{+0.6}_{-0.4}$	567^{+2}_{-2}
	B127	2000^{+1000}_{-1000}	2000^{+1000}_{-2000}	$0.19^{+0.06}_{-0.11}$	57645.465133243(7)	$0.8^{+0.4}_{-0.4}$	$1.2^{+0.6}_{-0.5}$	$566.0^{+1.9}_{-0.7}$
	B128†	1000^{+1000}_{-1000}	2700^{+900}_{-1500}	$0.25^{+0.05}_{-0.09}$	57645.466100959(6)	$1.1^{+0.2}_{-0.2}$	$0.9^{+0.3}_{-0.3}$	$567.0^{+0.7}_{-0.9}$
	B129	1710^{+1380}_{-20}	90^{+450}_{-30}	$0.11^{+4.56}_{-0.02}$	57645.466379997(5)	$1.0^{+0.3}_{-0.3}$	$1.3^{+0.4}_{-0.4}$	573^{+2}_{-3}
	B130†	2000^{+1000}_{-1000}	3000^{+1000}_{-1000}	$0.18^{+0.05}_{-0.05}$	57645.46833947(1)	$1.4^{+0.4}_{-0.4}$	$0.6^{+0.4}_{-0.2}$	$565.5^{+1.0}_{-0.8}$
	B131	1460^{+10}_{-10}	90^{+10}_{-10}	$0.08^{+0.01}_{-0.01}$	57645.47236212(1)	$1.1^{+0.4}_{-0.3}$	$0.7^{+0.3}_{-0.3}$	564^{+1}_{-2}
	B132	1720^{+80}_{-20}	100^{+70}_{-20}	$0.09^{+0.03}_{-0.01}$	57645.474138540(3)	$0.7^{+0.1}_{-0.1}$	$0.4^{+0.2}_{-0.2}$	561^{+1}_{-1}
	B133	1740^{+180}_{-50}	230^{+110}_{-40}	$0.22^{+0.1}_{-0.03}$	57645.474448229(4)	$1.7^{+0.2}_{-0.2}$	$0.7^{+0.3}_{-0.3}$	$570.6^{+0.7}_{-0.7}$

NOTE— 1σ errors on the fits are shown on superscript and subscript of each value in the table. For μ_t , the error on the last significant digit is shown in parenthesis.

^aBurst IDs are chronological. Individual component number (N) for multi-component bursts are appended to the burst IDs. Bursts modeled only using `curve_fit` are marked with *. We do not show the errors on these bursts as we found them to be unreliable and are under or overestimated. Bursts that extend beyond the observable bandwidth can also have unreliable estimates of spectra parameters and fluence (see Section 3.5.7). We mark those bursts with † to indicate that their fluence and spectra parameters could be unconstrained.

^b μ_t is the mean of the pulse profile in units of MJD. This can be considered as the arrival time of the pulse. It is referenced to the solar system barycenter, after correcting to infinite frequency using a DM of 560.5 pc cm⁻³.

Facilities: Arecibo

Software: Astropy (Astropy Collaboration et al. 2013; Price-Whelan et al. 2018), Numpy (Harris et al.

2020), Matplotlib (Hunter 2007), Pandas (Wes McKinney 2010; Reback et al. 2021), YOUR (Aggarwal et al. 2020), FETCH (Aggarwal et al. 2020a), Emcee (Foreman-

Mackey et al. 2013), ChainConsumer (Hinton 2016), SciencePlots (Garrett & Peng 2021)

REFERENCES

Agarwal, D., Aggarwal, K., Burke-Spolaor, S., Lorimer, D. R., & Garver-Daniels, N. 2020a, Monthly Notices of the Royal Astronomical Society, 497, 1661, doi: [10.1093/mnras/staa1856](https://doi.org/10.1093/mnras/staa1856)

Agarwal, D., Lorimer, D. R., Surnis, M. P., et al. 2020b, MNRAS, 497, 352, doi: [10.1093/mnras/staa1927](https://doi.org/10.1093/mnras/staa1927)

Aggarwal, K., Law, C. J., Burke-Spolaor, S., et al. 2020, Research Notes of the American Astronomical Society, 4, 94, doi: [10.3847/2515-5172/ab9f33](https://doi.org/10.3847/2515-5172/ab9f33)

Aggarwal, K., Agarwal, D., Kania, J. W., et al. 2020, Journal of Open Source Software, 5, 2750, doi: [10.21105/joss.02750](https://doi.org/10.21105/joss.02750)

Aggarwal, K., Burke-Spolaor, S., Law, C. J., et al. 2021, arXiv e-prints, arXiv:2104.07046. <https://arxiv.org/abs/2104.07046>

Astropy Collaboration, Robitaille, T. P., Tollerud, E. J., et al. 2013, Astronomy & Astrophysics, 558, A33, doi: [10.1051/0004-6361/201322068](https://doi.org/10.1051/0004-6361/201322068)

Barsdell, B. R. 2012, PhD thesis, Swinburne University of Technology

Bera, A., & Chengalur, J. N. 2019, MNRAS, 490, L12, doi: [10.1093/mnrasl/slz140](https://doi.org/10.1093/mnrasl/slz140)

Bhat, N. D. R., Cordes, J. M., Camilo, F., Nice, D. J., & Lorimer, D. R. 2004, ApJ, 605, 759, doi: [10.1086/382680](https://doi.org/10.1086/382680)

Bij, A., Lin, H.-H., Li, D., et al. 2021, arXiv e-prints, arXiv:2105.08851. <https://arxiv.org/abs/2105.08851>

Burke-Spolaor, S., Johnston, S., Bailes, M., et al. 2012, MNRAS, 423, 1351, doi: [10.1111/j.1365-2966.2012.20998.x](https://doi.org/10.1111/j.1365-2966.2012.20998.x)

Cheng, Y., Zhang, G. Q., & Wang, F. Y. 2020, MNRAS, 491, 1498, doi: [10.1093/mnras/stz3085](https://doi.org/10.1093/mnras/stz3085)

CHIME/FRB Collaboration, Amiri, M., Bandura, K., et al. 2019, Nature, 566, 235, doi: [10.1038/s41586-018-0864-x](https://doi.org/10.1038/s41586-018-0864-x)

CHIME/FRB Collaboration, Andersen, B. C., Bandura, K. M., et al. 2020, Nature, 587, 54, doi: [10.1038/s41586-020-2863-y](https://doi.org/10.1038/s41586-020-2863-y)

Chime/Frb Collaboration, Amiri, M., Andersen, B. C., et al. 2020, Nature, 582, 351, doi: [10.1038/s41586-020-2398-2](https://doi.org/10.1038/s41586-020-2398-2)

Connor, L., & van Leeuwen, J. 2018, AJ, 156, 256, doi: [10.3847/1538-3881/aae649](https://doi.org/10.3847/1538-3881/aae649)

Cordes, J. M., Wasserman, I., Hessels, J. W. T., et al. 2017, ApJ, 842, 35, doi: [10.3847/1538-4357/aa74da](https://doi.org/10.3847/1538-4357/aa74da)

Cruces, M., Spitler, L. G., Scholz, P., et al. 2020, Monthly Notices of the Royal Astronomical Society, 500, 448, doi: [10.1093/mnras/staa3223](https://doi.org/10.1093/mnras/staa3223)

Farah, W., Flynn, C., Bailes, M., et al. 2019, MNRAS, 488, 2989, doi: [10.1093/mnras/stz1748](https://doi.org/10.1093/mnras/stz1748)

Foreman-Mackey, D., Hogg, D. W., Lang, D., & Goodman, J. 2013, PASP, 125, 306, doi: [10.1086/670067](https://doi.org/10.1086/670067)

Gajjar, V., Siemion, A. P. V., Price, D. C., et al. 2018, ApJ, 863, 2, doi: [10.3847/1538-4357/aad005](https://doi.org/10.3847/1538-4357/aad005)

Garrett, J. D., & Peng, H.-H. 2021, doi: [10.5281/zenodo.4106649](https://doi.org/10.5281/zenodo.4106649)

Geyer, M., Serylak, M., Abbate, F., et al. 2021, arXiv e-prints, arXiv:2105.09096. <https://arxiv.org/abs/2105.09096>

Goodman, J., & Weare, J. 2010, Communications in Applied Mathematics and Computational Science, 5, 65, doi: [10.2140/camcos.2010.5.65](https://doi.org/10.2140/camcos.2010.5.65)

Gourdji, K., Michilli, D., Spitler, L. G., et al. 2019, The Astrophysical Journal, 877, L19, doi: [10.3847/2041-8213/ab1f8a](https://doi.org/10.3847/2041-8213/ab1f8a)

Gupta, V., Flynn, C., Farah, W., et al. 2021, MNRAS, 501, 2316, doi: [10.1093/mnras/staa3683](https://doi.org/10.1093/mnras/staa3683)

Harris, C. R., Millman, K. J., van der Walt, S. J., et al. 2020, Nature, 585, 357, doi: [10.1038/s41586-020-2649-2](https://doi.org/10.1038/s41586-020-2649-2)

He, K., Zhang, X., Ren, S., & Sun, J. 2015, arXiv e-prints, arXiv:1512.03385. <https://arxiv.org/abs/1512.03385>

Heintz, K. E., Prochaska, J. X., Simha, S., et al. 2020, ApJ, 903, 152, doi: [10.3847/1538-4357/abb6fb](https://doi.org/10.3847/1538-4357/abb6fb)

Hessels, J. W. T., Spitler, L. G., Seymour, A. D., et al. 2019, ApJL, 876, L23, doi: [10.3847/2041-8213/ab13ae](https://doi.org/10.3847/2041-8213/ab13ae)

Hinton, S. R. 2016, The Journal of Open Source Software, 1, 00045, doi: [10.21105/joss.00045](https://doi.org/10.21105/joss.00045)

Huijse, P., Estévez, P. A., Förster, F., et al. 2018, ApJS, 236, 12, doi: [10.3847/1538-4365/aab77c](https://doi.org/10.3847/1538-4365/aab77c)

Hunter, J. D. 2007, Computing in Science & Engineering, 9, 90, doi: [10.1109/MCSE.2007.55](https://doi.org/10.1109/MCSE.2007.55)

Karuppusamy, R., Stappers, B. W., & van Straten, W. 2010, A&A, 515, A36, doi: [10.1051/0004-6361/200913729](https://doi.org/10.1051/0004-6361/200913729)

Katz, J. I. 2018, Monthly Notices of the Royal Astronomical Society, 476, 1849, doi: [10.1093/mnras/sty366](https://doi.org/10.1093/mnras/sty366)

Keane, E. F., & Petroff, E. 2015, MNRAS, 447, 2852, doi: [10.1093/mnras/stu2650](https://doi.org/10.1093/mnras/stu2650)

Kirsten, F., Snelders, M. P., Jenkins, M., et al. 2021, Nature Astronomy, 5, 414, doi: [10.1038/s41550-020-01246-3](https://doi.org/10.1038/s41550-020-01246-3)

Kramer, M., Wielebinski, R., Jessner, A., Gil, J. A., & Seiradakis, J. H. 1994, A&AS, 107, 515

Kumar, P., Shannon, R. M., Osłowski, S., et al. 2019, ApJL, 887, L30, doi: [10.3847/2041-8213/ab5b08](https://doi.org/10.3847/2041-8213/ab5b08)

Kumar, P., Shannon, R. M., Flynn, C., et al. 2021, MNRAS, 500, 2525, doi: [10.1093/mnras/staa3436](https://doi.org/10.1093/mnras/staa3436)

Law, C. J., Abruzzo, M. W., Bassa, C. G., et al. 2017, ApJ, 850, 76, doi: [10.3847/1538-4357/aa9700](https://doi.org/10.3847/1538-4357/aa9700)

Law, C. J., Butler, B. J., Prochaska, J. X., et al. 2020, ApJ, 899, 161, doi: [10.3847/1538-4357/aba4ac](https://doi.org/10.3847/1538-4357/aba4ac)

Levin, L. 2012, PhD thesis, Swinburne University of Technology

Li, B., Li, L.-B., Zhang, Z.-B., et al. 2019, International Journal of Cosmology, Astronomy and Astrophysics, 1, 22, doi: [10.18689/ijcaa-1000108](https://doi.org/10.18689/ijcaa-1000108)

Luo, R., Wang, B. J., Men, Y. P., et al. 2020, Nature, 586, 693, doi: [10.1038/s41586-020-2827-2](https://doi.org/10.1038/s41586-020-2827-2)

Lyu, F., Meng, Y.-Z., Tang, Z.-F., et al. 2021, Frontiers of Physics, 16, 24503, doi: [10.1007/s11467-020-1039-4](https://doi.org/10.1007/s11467-020-1039-4)

McKinnon, M. M. 2014, PASP, 126, 476, doi: [10.1086/676975](https://doi.org/10.1086/676975)

Metzger, B. D., Margalit, B., & Sironi, L. 2019, MNRAS, 485, 4091, doi: [10.1093/mnras/stz700](https://doi.org/10.1093/mnras/stz700)

Michilli, D., Hessels, J. W. T., Lyon, R. J., et al. 2018, MNRAS, 480, 3457, doi: [10.1093/mnras/sty2072](https://doi.org/10.1093/mnras/sty2072)

Mickaliger, M. B., McLaughlin, M. A., Lorimer, D. R., et al. 2012, ApJ, 760, 64, doi: [10.1088/0004-637X/760/1/64](https://doi.org/10.1088/0004-637X/760/1/64)

Morello, V., Barr, E. D., Stappers, B. W., Keane, E. F., & Lyne, A. G. 2020, MNRAS, 497, 4654, doi: [10.1093/mnras/staa2291](https://doi.org/10.1093/mnras/staa2291)

Nita, G. M., & Gary, D. E. 2010, Monthly Notices of the Royal Astronomical Society, 406, L60, doi: [10.1111/j.1745-3933.2010.00882.x](https://doi.org/10.1111/j.1745-3933.2010.00882.x)

Oostrum, L. C., Maan, Y., van Leeuwen, J., et al. 2020, Astronomy & Astrophysics, 635, A61, doi: [10.1051/0004-6361/201937422](https://doi.org/10.1051/0004-6361/201937422)

Oppermann, N., Yu, H.-R., & Pen, U.-L. 2018, Monthly Notices of the Royal Astronomical Society, 475, 5109, doi: [10.1093/mnras/sty004](https://doi.org/10.1093/mnras/sty004)

Parent, E., Kaspi, V. M., Ransom, S. M., et al. 2018, ApJ, 861, 44, doi: [10.3847/1538-4357/aac5f0](https://doi.org/10.3847/1538-4357/aac5f0)

Pastor-Marazuela, I., Connor, L., van Leeuwen, J., et al. 2020, arXiv e-prints, arXiv:2012.08348, <https://arxiv.org/abs/2012.08348>

Patel, C., Agarwal, D., Bhardwaj, M., et al. 2018, ApJ, 869, 181, doi: [10.3847/1538-4357/aaee65](https://doi.org/10.3847/1538-4357/aaee65)

Petroff, E., & Chatterjee, S. 2021, Cornell University Library, doi: [10.7298/5N8E-XX87](https://doi.org/10.7298/5N8E-XX87)

Platts, E., Caleb, M., Stappers, B. W., et al. 2021, arXiv e-prints, arXiv:2105.11822, <https://arxiv.org/abs/2105.11822>

Pleunis, Z., Michilli, D., Bassa, C. G., et al. 2021, ApJL, 911, L3, doi: [10.3847/2041-8213/abec72](https://doi.org/10.3847/2041-8213/abec72)

Popov, M. V., & Stappers, B. 2007, A&A, 470, 1003, doi: [10.1051/0004-6361:20066589](https://doi.org/10.1051/0004-6361:20066589)

Price-Whelan, A. M., Sipőcz, B. M., Günther, H. M., et al. 2018, The Astronomical Journal, 156, 123, doi: [10.3847/1538-3881/aabc4f](https://doi.org/10.3847/1538-3881/aabc4f)

Rajwade, K. M., Mickaliger, M. B., Stappers, B. W., et al. 2020a, MNRAS, 493, 4418, doi: [10.1093/mnras/staa616](https://doi.org/10.1093/mnras/staa616)

—. 2020b, MNRAS, 495, 3551, doi: [10.1093/mnras/staa1237](https://doi.org/10.1093/mnras/staa1237)

Ransom, S. 2011, PRESTO: Pulsar Exploration and Search TOOlkit. <http://ascl.net/1107.017>

Reback, J., McKinney, W., Jbrockmendel, et al. 2021, pandas-dev/pandas: Pandas 1.2.1, Zenodo, doi: [10.5281/ZENODO.3509134](https://doi.org/10.5281/ZENODO.3509134)

Russakovsky, O., Deng, J., Su, H., et al. 2014, arXiv e-prints, arXiv:1409.0575, <https://arxiv.org/abs/1409.0575>

Shannon, R. M., Macquart, J. P., Bannister, K. W., et al. 2018, Nature, 562, 386, doi: [10.1038/s41586-018-0588-y](https://doi.org/10.1038/s41586-018-0588-y)

Simard, D., & Ravi, V. 2020, ApJL, 899, L21, doi: [10.3847/2041-8213/abaa40](https://doi.org/10.3847/2041-8213/abaa40)

Spitler, L. G., Cordes, J. M., Hessels, J. W. T., et al. 2014, The Astrophysical Journal, 790, 101, doi: [10.1088/0004-637x/790/2/101](https://doi.org/10.1088/0004-637x/790/2/101)

Spitler, L. G., Scholz, P., Hessels, J. W. T., et al. 2016, Nature, 531, 202, doi: [10.1038/nature17168](https://doi.org/10.1038/nature17168)

Tendulkar, S. P., Bassa, C. G., Cordes, J. M., et al. 2017, The Astrophysical Journal, 834, L7, doi: [10.3847/2041-8213/834/2/l7](https://doi.org/10.3847/2041-8213/834/2/l7)

Thulasiram, P., & Lin, H.-H. 2021, arXiv e-prints, arXiv:2105.13316, <https://arxiv.org/abs/2105.13316>

VanderPlas, J. T. 2018, The Astrophysical Journal Supplement Series, 236, 16, doi: [10.3847/1538-4365/aab766](https://doi.org/10.3847/1538-4365/aab766)

Wes McKinney. 2010, in Proceedings of the 9th Python in Science Conference, ed. Stéfan van der Walt & Jarrod Millman, 56 – 61, doi: [10.25080/Majora-92bf1922-00a](https://doi.org/10.25080/Majora-92bf1922-00a)

Zhang, Y. G., Gajjar, V., Foster, G., et al. 2018, The Astrophysical Journal, 866, 149, doi: [10.3847/1538-4357/aadf31](https://doi.org/10.3847/1538-4357/aadf31)